Core-collapse supernova neutrino emission and detection informed by state-of-the-art three-dimensional numerical models

Hiroki Nagakura,[1] Adam Burrows,[1] David Vartanyan [2]* and David Radice[3,4]

[1]*Department of Astrophysical Sciences, Princeton University, 4 Ivy Lane, Princeton, NJ 08544, USA*
[2]*Astronomy Department and Theoretical Astrophysics Center, University of California, Berkeley, CA 94720, USA*
[3]*Department of Physics, The Pennsylvania State University, University Park, PA 16802, USA*
[4]*Department of Astronomy and Astrophysics, The Pennsylvania State University, University Park, PA 16802, USA*

ABSTRACT

Based on our recent three-dimensional core-collapse supernova (CCSN) simulations including both exploding and non-exploding models, we study the detailed neutrino signals in representative terrestrial neutrino observatories, namely Super-Kamiokande (Hyper-Kamiokande), DUNE, JUNO, and IceCube. We find that the physical origin of difference in the neutrino signals between 1D and 3D is mainly proto-neutron-star convection. We study the temporal and angular variations of the neutrino signals and discuss the detectability of the time variations driven by the spiral standing accretion shock instability (spiral SASI) when it emerges for non-exploding models. In addition, we determine that there can be a large angular asymmetry in the event rate ($\gtrsim$50 per cent), but the time-integrated signal has a relatively modest asymmetry ($\lesssim$20 per cent). Both features are associated with the lepton-number emission self-sustained asymmetry and the spiral SASI. Moreover, our analysis suggests that there is an interesting correlation between the total neutrino energy (TONE) and the cumulative number of neutrino events in each detector, a correlation that can facilitate data analyses of real observations. We demonstrate the retrieval of neutrino energy spectra for all flavours of neutrino by applying a novel spectrum reconstruction technique to the data from multiple detectors. We find that this new method is capable of estimating the TONE within the error of $\sim$20 per cent if the distance to the CCSN is $\lesssim$6 kpc.

Key words: neutrinos – supernovae: general.

1 INTRODUCTION

A core-collapse supernova (CCSN) arises from a catastrophic death of a massive star ($M \gtrsim 8\,\mathrm{M_\odot}$). During the development of the explosion and the cooling of the proto-neutron star (PNS), a total energy of $\sim$3 × 10^{53} erg is radiated. Indeed, a neutrino burst associated with a CCSN was directly detected from SN 1987A by the terrestrial neutrino detectors Kamiokande (Hirata et al. 1987) and the IMB (Irvine–Michigan–Brookhaven) (Bionta et al. 1987). They detected a total of 19 events with neutrino energies ranging from $\sim$5 to $\sim$40 MeV and the event lasted $\sim$10 s; this is consistent with our understanding of the dynamics of CCSN, albeit very crudely. On the other hand, due to the low number of events and poor flavour sensitivity, these observations did not provide enough information to constrain the explosion mechanism. This is a major opportunity for the future.

A large number of neutrino detectors with sensitivities to multiple neutrino flavours should be available when the next galactic CCSN happens. Super-Kamiokande (SK), one of the currently operating water-Cherenkov neutrino detectors, is capable of detecting $\sim$10 000 neutrinos from a CCSN at the distance of 10 kpc (Abe et al. 2016); Hyper-Kamiokande (HK) is essentially a scaled-up version of SK by a factor of several in volume (Hyper-Kamiokande Proto-Collaboration 2018) and the project has recently been officially approved. The deep underground neutrino experiment (DUNE) is a liquid-Argon detector that will have a unique sensitivity to electron-type neutrinos (ν_e; Acciarri et al. 2016; Ankowski et al. 2016). The Jiangmen Underground Neutrino Observatory (JUNO), one of the upcoming liquid-scintillator detectors, is designed mainly to determine the neutrino mass hierarchy by a precise measurement of reactor antineutrino spectra, but this capability is also useful for detecting CCSN neutrinos (An et al. 2016). Due to its large effective mass, IceCube will detect $\sim$100 times the number of neutrino events that SK will (Abbasi et al. 2011).[1] Taking advantage of these facilities, the time structures and flavour-dependent features in neutrino signals are available for observation, and such data can help us understand not only CCSN dynamics, but neutrino flavour conversion in CCSN cores.

CCSN dynamics is governed by the complex interplay between microphysics and macrophysics, which engenders rich structures in its neutrino signal. With a future direct detection of supernova neutrinos, the complex features therein encoded will be best studied by comparing with theoretical predictions of the signals obtained by the sophisticated numerical simulations. There have been many such studies (see e.g. Scholberg 2012; O'Connor & Ott 2013; Li et al. 2019; Suwa et al. 2019; Warren et al. 2019), and groups have used either their own CCSN simulations or publicly available

---

[1]We refer readers to, e.g. Scholberg (2012) and references therein for other available methodologies capable of addressing the detection of CCSN neutrinos.

* E-mail: dvartany@berkeley.edu

models (Hüdepohl et al. 2010; Nakazato et al. 2013). However, these neutrino data generally derive from spherically symmetric CCSN simulations. More importantly, such 1D studies generally employ artificial means to explode the model and to determine when to explode it (see Hüdepohl et al. 2010, for an exception). Such an approach is unavoidable, since shocks do not generally revive in state-of-the-art 1D simulations. It is therefore preferable when developing theoretical predictions of neutrino signals to conduct multidimensional simulations for which explosion is a common outcome.

In this paper, we present the first systematic study of neutrino signals based on our 3D CCSN simulations. Although previously there have been a few explorations of the neutrino emissions from 3D models (see e.g. Takiwaki & Kotake 2018; Glas et al. 2019; Müller 2019; Vartanyan, Burrows & Radice 2019; Walk et al. 2019, 2020), little has been studied of the differences between 3D and 1D models in a detector. In this paper, we develop a new analysis pipeline by employing and extending the SNOWGLOBES detector software[2] and we discuss the unique characteristics of 3D models, in particular their expected neutrino event rate, energy spectrum, angular dependences, and time variation. We use the FORNAX code (Skinner et al. 2019) in our 3D CCSN simulations. FORNAX incorporates the important neutrino–matter interactions and multigroup neutrino transport, taking into account the fluid-velocity dependence and general-relativistic redshifts. The relatively speedy FORNAX code has allowed us to conduct many CCSN simulations across a wide range of massive-star progenitors, with both exploding and non-exploding outcomes. Although these CCSN models are still provisional and need further improvements, the essential characteristics of the progenitor dependence may have been captured adequately. All the numerical neutrino data we use in this paper are publicly available.[3]

This paper is organized as follows: In Section 2, we briefly summarize our numerical CCSN models. We then provide basic information for calculating neutrino signals in the detector for normal-hierarchy and inverted-hierarchy neutrino oscillation models. All results of our analysis are presented in Section 3. Finally, in Section 4 we wrap up with a summary and conclusions.

2 METHODS AND MODELS

2.1 3D CCSN models

All technical details of the FORNAX code that we employed to generate our 3D CCSN models have been published in a series of papers (Skinner, Burrows & Dolence 2016; Radice et al. 2017; Vartanyan et al. 2018; Skinner et al. 2019). We refer readers to Burrows, Radice & Vartanyan (2019) and Burrows et al. (2020) for a detailed discussion of these 3D models, Vartanyan et al. (2019) for an exploration of the temporal and angular variations of the neutrino signals, and Nagakura et al. (2020) for an analysis of PNS convection.

At the onset of collapse, our CCSN simulations are performed in spherical symmetry by taking a matter profile computed by stellar evolution models. In this study, we include the results for 9-, 10-, 12-, 13-, 14-, 15-, 19-, and 25-$M_\odot$ models (eight models in total), enough to blanket the overall progenitor dependence.[4] The initial 1D models were calculated by Sukhbold et al. (2016), except for the 25-$M_\odot$ progenitor that was calculated by Sukhbold, Woosley & Heger (2018). Once the simulation reached 10 ms after core bounce,

[2]See https://webhome.phy.duke.edu/~schol/snowglobes/ for more details.
[3]From the link https://www.astro.princeton.edu/~burrows/.
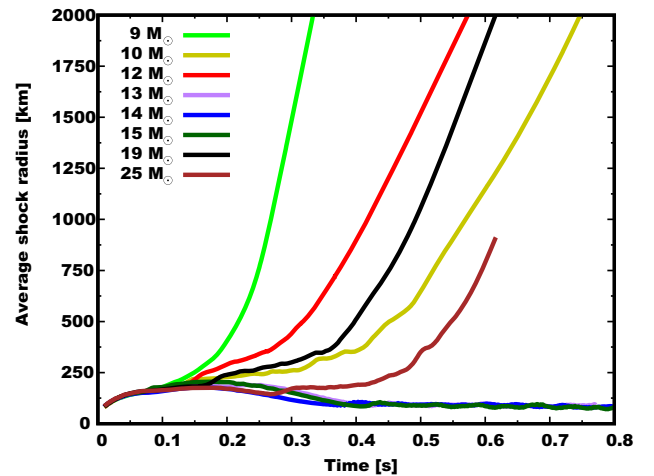[4]All progenitor models employed in this paper are non-rotating models.

Figure 1. The time evolution of the mean shock radius for 3D models upon which we focus in this paper. Colour distinguishes the ZAMS mass of the progenitor.

we mapped both matter and neutrino radiation profiles to 3D and imposed non-radial perturbations in the fluid velocity following the prescription in Müller & Janka (2015). We employed a spherical coordinate, dendritic mesh with $678 \times 128 \times 256$ ($r \times \theta \times \phi$) grid points covering $0 \le r \le 20\,000$ km. The radial grid is logarithmically stretched outside the inner ~ 70 km.

The neutrino transport module in FORNAX solves the energy-dependent two moment equations for three neutrino species: electron-type neutrinos ν_e, electron-type antineutrinos $\bar{\nu}_e$, and all the other heavy neutrinos bundled into what we call 'ν_x.' The fluid-velocity dependence is included up to $\mathcal{O}(v/c)$ and the effect of general relativity is approximately included using the scheme in Rampp & Janka (2002). We use 12 energy groups that are logarithmically distributed from 1 to 300 MeV for ν_e and from 1 to 100 MeV for the other species. (We note that we display the result of 1D simulation for comparison, in which we employ 20 energy groups for them. The energy-resolution dependence in 1D models is also displayed in Appendix A.) The transport equation is solved with up-to-date neutrino–matter interactions detailed in Burrows, Reddy & Thompson (2006), adding recent improvements, e.g. many body corrections (Horowitz et al. 2017). Other modules such as hydrodynamics (and gravity) are solved simultaneously with neutrino transport and energy, momentum, and lepton number coupling in fully and self-consistently included each (see Skinner et al. 2019, for more details).

We witnessed successful explosions for the 9-, 10-, 12-, 19-, and 25-$M_\odot$ models (i.e. the 13-, 14-, and 15-$M_\odot$ models did not explode). These outcomes are collectively demonstrated via the time trajectories of the mean shock radii displayed in Fig. 1. As is clearly seen, the explodability and the vigour of shock expansion are not monotonic functions of Zero Age Main Sequence (ZAMS) mass. It is important to note that the 9-$M_\odot$ model is launched earliest ($\lesssim 150$ ms after bounce) and that hydrodynamic instabilities did not have much time to grow to full vigour. Indeed, its explosion geometry is nearly spherical and the multidimensional effects for this model are not pronounced. However, we found that, despite the near sphericity of the blast, the neutrino emissions of the 9-$M_\odot$ model are asymmetric (Vartanyan et al. 2019). The other models have different CCSN dynamics. For them, neutrino-driven convection is well developed prior to explosion (if the model explodes). The associated increase
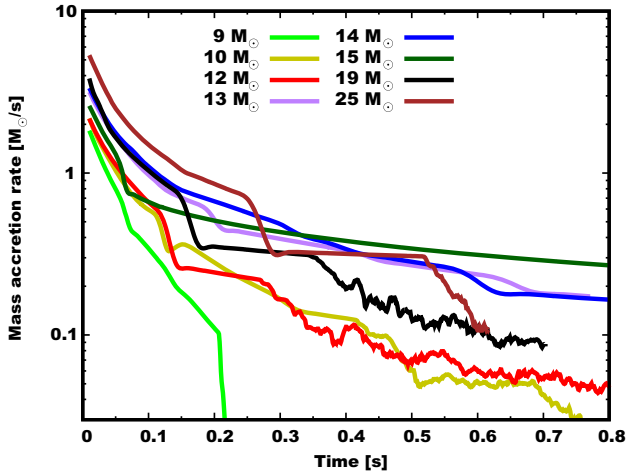
Figure 2. The time evolution of the mass accretion rate measured at 500 km.

in the turbulent pressure and neutrino heating rate can help facilitate shock expansion.

We point out some important features that can be realized only in 3D models. Shock revival is not achieved in 1D models; hence, previous studies have needed to use artificial prescriptions when studying the neutrino signals of CCSN models. For instance, in Nakazato et al. (2013) shock revival is assumed to take place at a certain time, at which time the simulations are mapped to those of PNS cooling. In this prescription, mass accretion on to the PNS is artificially shut off. As shown in Fig. 2, mass accretion continues after shock revival, supplying mass and power to the PNS and influencing the neutrino emissions quantitatively. Another crucial deficiency of 1D models is that PNS convection is suppressed. In our previous paper (Nagakura et al. 2020), we confirmed that PNS convection commonly occurs for all stellar collapses within the mass range explored, including not only exploding models, but also their failed counterparts. The latter would go through the PNS phase, but subsequently collapse to a black hole. We find that PNS convection substantially affects both the neutrino luminosity and average neutrino energy (see Fig. 3). This is mainly attributed to the fact that the convection changes the quasi-hydrostatic structure of the core and expands the neutrinospheres. These adjustments change the thermodynamic state and thereby affect neutrino emissions (see section 3.4 in Nagakura et al. 2020, for more details). Although convection can be treated approximately in 1D simulations with a mixing length theory (see e.g. Roberts et al. 2012), such an approach can provide only crude qualitative trends and may not be very accurate. It is also important to note that the lepton-number emission self-sustained asymmetry (LESA; Tamborra et al. 2014) is also observed in 3D models and that this is tied to the derived directional variations of the theoretical neutrino signals. Furthermore, we have found that the spiral standing accretion shock instability (spiral SASI; Blondin & Shaw 2007) appears in non-exploding models and that this induces temporal modulation of the neutrino signal and asymmetric neutrino emission. As such, our 3D models capture key multidimensional features unavailable using 1D models. We delve into the observational consequences in Section 3.

2.2 Detectors

For this study, we employ the SNOWGLOBES detector software to estimate neutrino event rates and energy spectra in each detector:

SK (HK), DUNE, JUNO, and IceCube. This software is publicly available, and it has been widely used by the cognizant community. In this section, we briefly summarize some essential properties of each detector installed in SNOWGLOBES and refer readers to Scholberg (2012) and Seadrow et al. (2018) for a more detailed discussion.

SK is a currently operating water Cherenkov neutrino detector, and we assume that its volume is 32.5 ktons for the purpose of CCSN neutrino analysis. It is sensitive primarily to $\bar{\nu}_e$s through the inverse-beta-decay reaction on protons (IBD-p):

$$\bar{\nu}_e + p \rightarrow e^+ + n. \tag{1}$$

Elastic scattering on electrons (eES),

$$\nu_i + e^- \rightarrow \nu_i + e^-, \tag{2}$$

is sensitive to all neutrino species, and can be employed to retrieve the neutrino energy spectra of all flavours of neutrinos emitted at the CCSN source (see Section 3.5 for more details). Although we employ only IBD-p and eES reaction channels in this study, there are other useful reaction channels for the study of CCSN neutrinos. Another IBD reaction, this with oxygen,

$$\bar{\nu}_e + {}^{16}O \rightarrow e^+ + {}^{16}N, \tag{3}$$

is capable of detect tagging $\bar{\nu}_e$s, and the charged-current reaction with oxygen is sensitive to ν_es through the reaction

$$\nu_e + {}^{16}O \rightarrow e^- + {}^{16}F. \tag{4}$$

We note that all neutrino species experience inelastic scattering with oxygen via the neutral-current reaction

$$\nu_i + {}^{16}O \rightarrow \nu_i + {}^{16}O^*, \tag{5}$$

in which the gamma-rays emitted upon the deexcitation of oxygen are detectable.

DUNE is a neutrino detector to emerge in mid-decade which employs a 40 kton liquid Time Projection Chamber based on liquid argon. The detector is most sensitive to ν_es via the charged-current reaction with argon (CCAre):

$$\nu_e + {}^{40}Ar \rightarrow e^- + {}^{40}K^*, \tag{6}$$

and is capable of detecting several thousands of ν_es from a CCSN at a distance of 10 kpc. We note that another charged-current reaction:

$$\bar{\nu}_e + {}^{40}Ar \rightarrow e^+ + {}^{40}Cl^*, \tag{7}$$

is sensitive to $\bar{\nu}_e$, although the event rate is subdominant due to its smaller ν_e cross-section. In this study, we focus only on the CCAre channel and ignore others. We note, however, that other channels may still be useful. For instance, coherent scattering with Ar via neutral-current reactions has the potential to provide information on all flavours of neutrinos, although there remain many technical issues to be studied (see e.g. Bian 2015; Nunez et al. 2017).

JUNO is a liquid-scintillator detector, which is planned for operation in 2021. It will have a volume of 20 ktons, and will be most sensitive to $\bar{\nu}_e$s via the IBD-p reaction. Although we use only the IBD-p reaction channel in this study, there are other charged-current reactions. These include

$$\bar{\nu}_e + {}^{12}C \rightarrow e^+ + {}^{12}B, \tag{8}$$

$$\nu_e + {}^{12}C \rightarrow e^- + {}^{12}N, \tag{9}$$

the neutral-current reaction on carbon

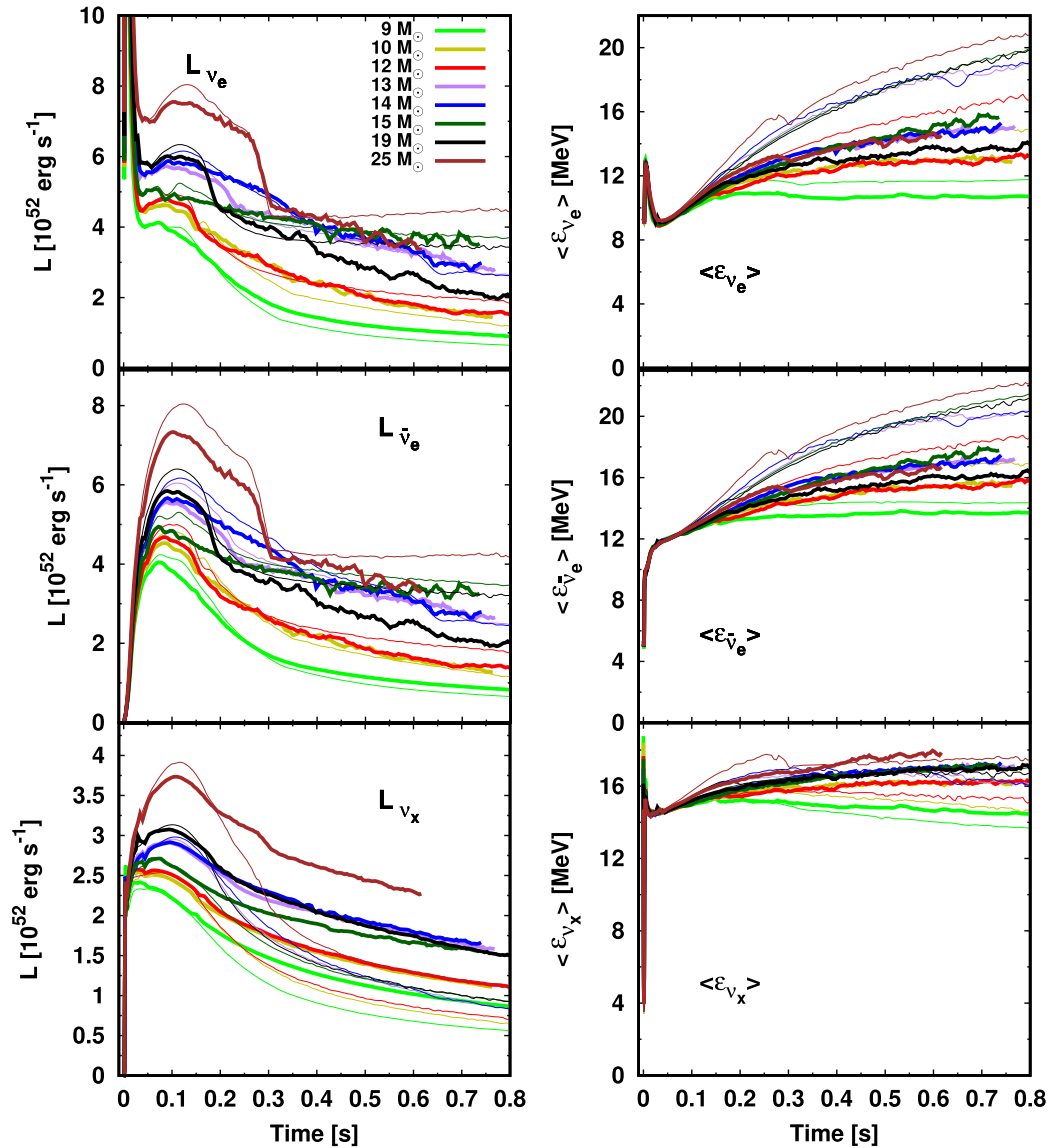$$\nu_i + {}^{12}C \rightarrow \nu_i + {}^{12}C^*, \tag{10}$$

Figure 3. The energy luminosity (left) and average neutrino energy (right) as a function of time for each species of neutrino for all 3D models in this study. These are measured in the laboratory frame at 250 km. For comparison, we display 1D counterparts as thin lines.

and with protons,

$$\nu_i + p \rightarrow \nu_i + p. \tag{11}$$

All these reactions can in principle be useful for studying CCSN neutrinos. As discussed in Beacom, Farr & Vogel (2002), those reaction channels may play an important role in retrieving the energy spectra for all neutrino flavours, although the systematic errors may be quite large (Li et al. 2019).

IceCube resides in Antarctica, is a few Mtonnes of pure water ice, and is primarily designed to detect $\gtrsim$100 GeV neutrinos. As pointed out early by Pryor, Roos & Webster (1988) and Halzen, Jacobsen & Zas (1996), this type of detector is also capable of detecting $\sim$MeV neutrinos by taking advantage of the large number of optical modules. Indeed, IceCube has many sensors constructed with a lattice of 5160 digital optical modules containing photomultiplier tubes. They are sensitive to Cherenkov photons produced mainly by IBD reactions, indicating that the collective photomultiplier rate will rise once a burst of $\bar{\nu}_e$ courses through the ice volume (Abbasi et al. 2011; Köpke & IceCube Collaboration 2011; Cross, Fritz &

Griswold 2019). By virtue of the large volume of the detector, $\sim$10^6 events are expected to be detected for a CCSN at a distance of 10 kpc. Although there are some systematic uncertainties in detector sensitivity (see e.g. Abbasi et al. 2011, for more details), we assume 100 per cent efficiency for event detection with a 3.5-Mtonne fiducial volume (Seadrow et al. 2018). In Section 3.3, we discuss the detectability of the spiral SASI in the IceCube data with the assumption that the background noise is 1.48×10^3 ms^{-1} (see e.g. Abbasi et al. 2011; Tamborra et al. 2013, for more details).

2.3 Neutrino oscillations

There has been accumulating experimental evidence for neutrino oscillations, implying that CCSN neutrinos undergo flavour conversion. In this paper, we employ a simplified approach, assuming a purely adiabatic Mikheyev–Smirnov–Wolfenstein (MSW) oscillation model for both normal and inverted neutrino-mass hierarchies. We ignore other possible matter effects, such as non-adiabaticity

(Kuo & Pantaleone 1989; Dighe & Smirnov 2000) and the effects of Earth's matter (Lunardini & Smirnov 2001). Also, we do not distinguish ν_μ, ν_τ, and their antiparticles at the CCSN source in our computations of flavour mixing, an approach that is consistent with our CCSN simulations. However, we distinguish neutrinos and antineutrinos at the Earth (see equations 12–15 for more details). It should also be mentioned that we do not take into account effects of neutrino–neutrino self-interaction in either our CCSN models or neutrino propagation, although this assumption may not be adequate. The occurrence of fast pairwise flavour conversion in CCSNe has recently been suggested (Abbar et al. 2019; Nagakura et al. 2019c; Delfan Azari et al. 2020; Morinaga et al. 2020) and extensive studies have been undertaken (see e.g. Shalgar & Tamborra 2019; Abbar 2020; Bhattacharyya & Dasgupta 2020; Glas et al. 2020; Johns et al. 2020). We postpone the incorporation of these effects to the future.

By introducing the neutrino survival probabilities p and $\bar{p}$ for neutrinos and their antiparticles, respectively, the neutrino and antineutrino fluxes at the Earth (F_i and $\bar{F}_i$, respectively) can be written as (see also Dighe & Smirnov 2000)

$$F_e = p F_e^0 + (1-p) F_x^0, \tag{12}$$

$$\bar{F}_e = \bar{p} \bar{F}_e^0 + (1-\bar{p}) \bar{F}_x^0, \tag{13}$$

$$F_x = \frac{1}{2}(1-p) F_e^0 + \frac{1}{2}(1+p) F_x^0, \tag{14}$$

$$\bar{F}_x = \frac{1}{2}(1-\bar{p}) \bar{F}_e^0 + \frac{1}{2}(1+\bar{p}) \bar{F}_x^0, \tag{15}$$

where F_i^0 and $\bar{F}_i^0$ denote the neutrino and antineutrino fluxes, respectively, in the case without flavour conversion. The subscript i represents the neutrino flavour, while x denotes either the μ- or τ-neutrino, i.e. $F_x = F_\mu = F_\tau$. Note that we assume in our CCSN models that these heavy leptonic neutrinos and their antipartners are identical at the source, i.e. $F_x^0 = \bar{F}_x^0$ (see Section 2.1). On the other hand, we distinguish them at the Earth, i.e. $F_x \neq \bar{F}_x$, since F_e^0 is different from $\bar{F}_e^0$, implying that heavy leptonic neutrinos and their antipartners are, in general, no longer identical to each other. As we shall discuss in Section 3.5, it is necessary to distinguish them to retrieve the neutrino spectra at the CCSN source from observed quantities, since the cross-section of the eES reaction is different between neutrinos and their antipartners. This treatment is different from other previous studies in the literature, including ours (Seadrow et al. 2018).

In the case of the normal-mass hierarchy, the survival probabilities can be written as

$$p = \sin^2\theta_{13}, \tag{16}$$

$$\bar{p} = \cos^2\theta_{12}\cos^2\theta_{13}. \tag{17}$$

For the inverted-mass hierarchy, they are

$$p = \sin^2\theta_{12}\cos^2\theta_{13}, \tag{18}$$

$$\bar{p} = \sin^2\theta_{13}. \tag{19}$$

In this study, we adopt the neutrino mixing parameters, θ_{12} and θ_{13} from Capozzi et al. (2017): $\sin^2\theta_{12} = 2.97 \times 10^{-1}$ and $\sin^2\theta_{13} = 2.15 \times 10^{-2}$.

3 RESULTS

3.1 Progenitor dependence

Unless otherwise stated, the central results we present in this paper assume a CCSN source distance of $d = 10$ kpc. Fig. 4 displays the time evolution of the angle-averaged event rate in the major channel of each detector: IBD-p for SK and JUNO, and CCAre for DUNE. We select four representative 3D models (9-, 13-, 19-, and 25-$M_\odot$) to highlight some qualitative trends with progenitor. For comparison, we also show the results of their corresponding 1D counterparts as thin lines, and the colour distinguishes neutrino oscillation models.

We confirm that DUNE has a unique sensitivity to the neutrino-mass hierarchy through the detection of neutronization burst ($T \lesssim 20$ ms), which is less dependent on progenitor (as suggested previously; see also Fig. 5). Up to the $T \sim 100$ ms, there are no remarkable differences between 1D and 3D, and the progenitor dependence is modest. However, by this time hydrodynamic instabilities have already emerged in the post-shock region. Prompt convection occurs at $T \lesssim 40$ ms, which provides major perturbations for neutrino-driven convection (see e.g. Nagakura et al. 2018), and non-radial motions behind the shock wave rapidly grow (see Nagakura et al. 2019a; Burrows et al. 2020, for more details). Nevertheless, our results suggest that multidimensional instabilities in the early post-bounce phase have less influence on the neutrino signals. This is mainly attributed to two facts: (1) the angle-averaged hydrodynamic quantities in 3D CCSN models are not so much different from those in 1D and (2) most of the convective region resides in optically thick regions, suggesting that multidimensional effects on neutrino signals are masked. We note, however, that low-energy neutrinos ($\lesssim 10$ MeV) can escape from the convective region due to their smaller interaction cross-sections. This indicates that multidimensional effects can be investigated using the few-MeV neutrinos, although it is not easy to detect them (since those neutrinos are also transparent to the detector medium). The improved sensitivity in liquid-scintillator detectors such as Borexino (BOREXINO Collaboration 2009), KamLAND (Asakura et al. 2016), SNO+ (SNO + Collaboration 2015), and JUNO for the few-MeV neutrinos may help with such an analysis. SK may also be capable at these lower energies (Simpson et al. 2019), although it would suffer from the low statistical significance.

At $T \gtrsim 100$ ms, on the other hand, remarkable progenitor and dimensional dependences emerge. Regardless of detector or neutrino oscillation model, we find that the event rate is lowest and highest for the 9 and 25 $M_\odot$ progenitors, respectively. This mainly reflects their different accretion histories. Indeed, the neutrino luminosities and event rates for different CCSN models are clearly correlated with mass accretion rate (see Fig. 2). This trend is consistent with previous studies based on 1D CCSN models (see e.g. Suwa et al. 2019). We note, however, that the detailed progenitor dependence cannot be captured adequately by 1D models, and we discuss this below.

We start with SK and JUNO results. As described in Section 2.3, these detectors are most sensitive to $\bar{\nu}_e$ neutrinos (at the Earth). We find that the event rate in 1D models is systematically higher than that in 3D in the case with no flavour conversion (red lines in Fig. 4). One might think that this is simply due to the failure of shock revival for 1D models in which the accretion component of neutrino luminosity is higher and the event rate is increased accordingly. This explanation is qualitatively true, but it is not enough to explain the difference. For instance, we find that the 13-$M_\odot$ model in 3D has a smaller event rate than that in 1D, in spite of the failure of shock revival for both cases. Where does the difference come from?
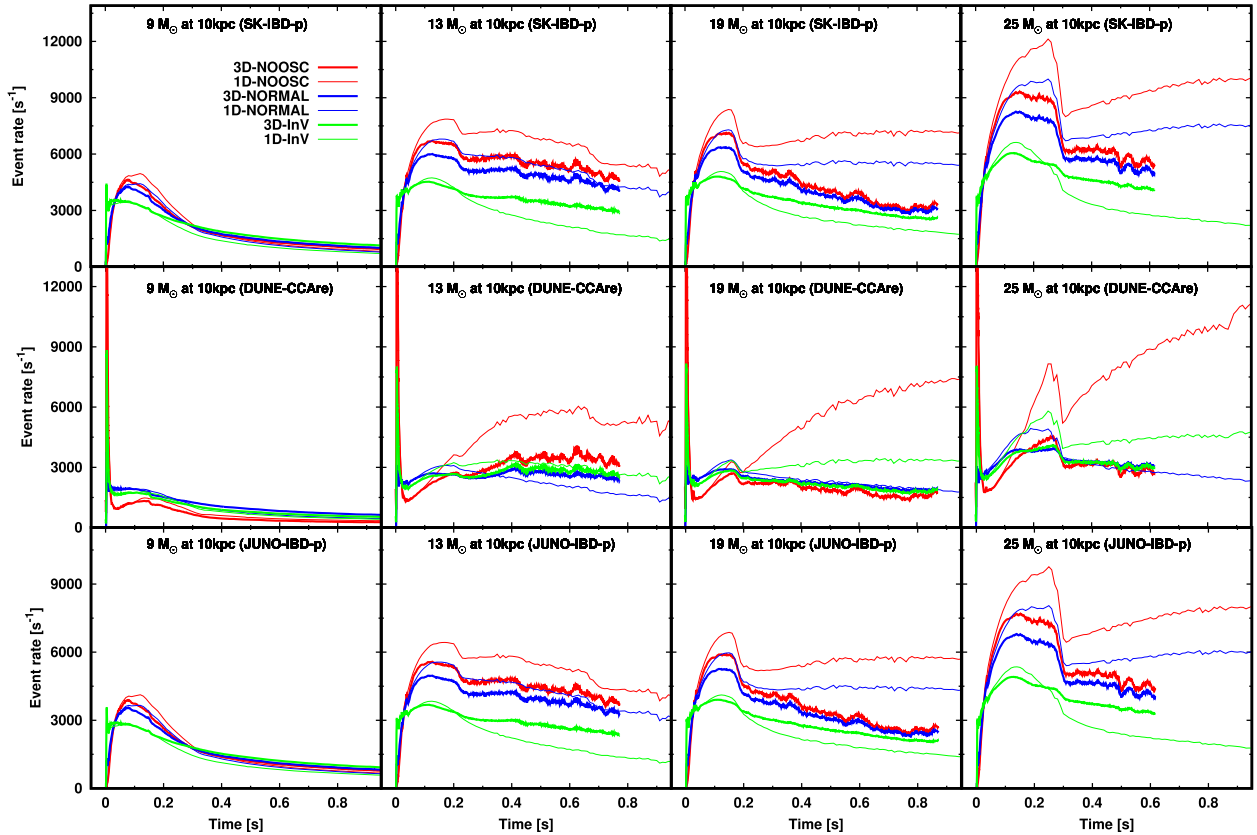
Figure 4. The time evolution of angle-averaged neutrino event rate detected through the major channel for each detector (from top to bottom, SK, DUNE, and JUNO) for selected models (from left to right, 9-, 13-, 19-, and 25-$M_\odot$). The colour distinguishes the neutrino oscillation model: no flavour conversions (red), normal-mass hierarchy (blue), and inverted-mass hierarchy (green). For comparison, we also display 1D counterparts as thin lines. The distance to the CCSN source is assumed to be 10 kpc.

A clue to understanding the difference is related to the average energy of $\bar{\nu}_e$ neutrinos at the source, which is shown in the right-hand and middle panels of Fig. 3. As shown, the average energy is systematically higher in 1D than 3D, which results in higher event rates for $\bar{\nu}_e$ neutrinos in SK and JUNO. As already mentioned in Section 2.1, PNS convection affects neutrino emission through its effect on the neutrinospheres. Due to PNS convection, the angle-averaged neutrinospheres in 3D are located at larger radii and lower matter temperatures than those in 1D. The latter effect reduces the average energy of $\bar{\nu}_e$ neutrinos in 3D, and this accounts for much of the difference in neutrino detection rates. The same trend can also be seen for event rates in DUNE (sensitive to ν_e neutrinos at the Earth), which is higher in 1D than 3D for no-oscillation models (see the middle panel of Fig. 4).

We now turn our attention to the case of the normal-mass hierarchy (blue lines in Fig. 4), for which the survival probability of $\bar{\nu}_e$ neutrinos is ~ 70 per cent. This indicates that the characteristics of $\bar{\nu}_e$ neutrinos at the CCSN source are still responsible for the major trends in the event rates at SK and JUNO. We find that the difference in the event rate between 1D and 3D models follows the same trend (however modest) as found in the case with no flavour conversions. On the other hand, the survival probability of ν_e neutrinos for the normal-mass hierarchy is almost zero, implying that the event rates at DUNE reflect the characteristics of ν_x neutrinos at the CCSN source. Since the ν_x luminosity is lower than that for ν_e neutrinos at the CCSN source, the event rate becomes smaller than that with no flavour conversions. We find that there are no remarkable differences in the event rates between 1D and 3D for all progenitor models at DUNE.

At first glance, this looks a bit strange, since the luminosity of ν_x neutrinos at the source is systematically higher in 3D than that in 1D (due to effects of PNS convection), while the average energy is very similar for the two cases (see Fig. 3).

This complexity can be illuminated by studying high-energy ν_x neutrinos at the source. Some fractions of ν_xs emitted in the vicinity of PNS experience shock acceleration, which creates a non-thermal tail in the energy spectrum (Hotokezaka and Nagakura, in preparation). The smaller shock radius that accompanies high mass accretion rates provides conducive conditions for shock acceleration actually realized in our 1D models (except for the 9-$M_\odot$ model). Although non-thermal neutrinos have a smaller contribution to luminosity and average energy, they affect the neutrino event rate at terrestrial detectors, perhaps in measurable ways. We emphasize that high-energy neutrino emission in the 9-, 19-, and 25-$M_\odot$ models in 3D is subtle, since the shock wave is revived and propagates through a low-density medium, making neutrino acceleration inefficient. The increase in neutrino event rate due to a non-thermal component in 1D compensates for the reduction in the event rate due to the absence of PNS convection. Hence, the dimensional dependence is not remarkable for these progenitors. On the other hand, the shock wave stalls and is not revived for the 3D model of 13-$M_\odot$, i.e. non-thermal neutrinos can contribute to its event rate. As a result, due to PNS convection the event rate is higher in 3D than that in 1D.[5]

---

[5]It should be noted that the contribution of the high-energy component in the 3D model is smaller than that of 1D. This is mainly because the shock
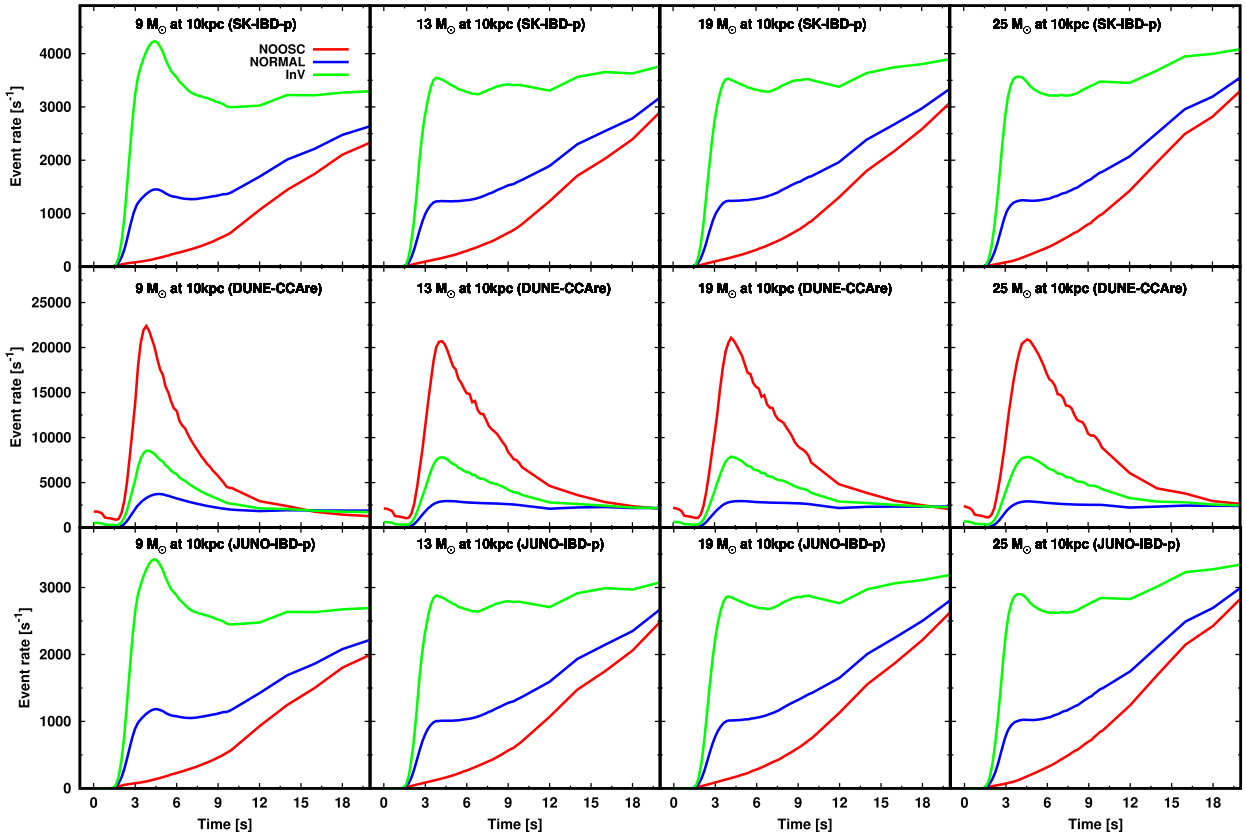
Figure 5. The same as Fig. 4 but focusing only in the earlier phase ($T < 20$ ms). Since the difference between 1D and 3D is subtle, we only display the result of 1D in this figure.

We now remark on the non-thermal component of ν_x neutrinos. As pointed out by Langanke et al. (2008), inelastic neutrino-nucleus scatterings may suppress the high-energy tail of the neutrino spectrum. Our CCSN simulations, however, do not incorporate the inelasticity in this reaction, though the velocity dependence and Doppler effects are included. If the non-thermal component is suppressed, the event rate of 1D models would be systematically smaller than that we obtain. We also note that accurate computations of shock acceleration require high-resolution neutrino transport simulations in both real and moment spaces, and neutrino transport with multi-angle treatment is also highly desired. Thus, we stress that there remain many uncertainties in the high-energy tail of ν_x neutrinos, which will be addressed in the future. It should be noted, however, that those uncertainties do not influence the event rates for our 3D CCSN models, in particular for successful explosions, since the shock alteration of the high-energy tail of the ν_x spectrum is negligible.

In the case of the inverted-mass hierarchy (green lines in Fig. 4), we find that the difference between 1D and 3D models in the event rates in SK and JUNO is modest. In the oscillation model, the event rate reflects the property of $\bar{\nu}_x$ neutrinos at the CCSN source. As in the case in DUNE for the normal-mass hierarchy, the non-thermal component of $\bar{\nu}_x$ neutrinos contributes interestingly to the 1D event rates. It should be noted, however, that the IBD-p cross-section is less sensitive to the neutrino energy than that for the CCAre, implying that the contribution from high-energy components is more modest

in SK and JUNO than in DUNE. As a result, the increase of the $\bar{\nu}_x$ luminosities due to PNS convection directly accounts for the higher event rate in SK and JUNO when comparing 3D and 1D, regardless of progenitor. On the other hand, the difference between the 1D and 3D event rates in DUNE can be explained by the same mechanism as in the case with the normal-mass hierarchy. For the inverted-mass hierarchy, the survival probability of ν_e neutrinos is ~ 30 per cent, implying that ν_x neutrinos at the source significantly affect the event rate. We find that the event rate is systematically higher in 1D than 3D for the 19- and 25-$M_\odot$ models, which is mainly due to the contribution of the high-energy ν_x neutrinos. We emphasize that the CCAre reaction has a higher sensitivity to high-energy neutrinos than does the IBD, with the result that the effects of the non-thermal tail in DUNE may be substantial. We also note that the difference for 13-$M_\odot$ model between 3D and 1D is modest, since non-thermal neutrinos are created in the 3D model and the shock fails.

Summarizing the above results, the details of the progenitor dependence and the difference between 1D and 3D models are determined by a complex interplay. At SK and JUNO, the event rate in 1D is systematically overestimated (underestimated) for the case with the normal(inverted)-mass hierarchy. For DUNE, the event rate is overestimated for the 1D case with the inverted-mass hierarchy, while the dimensional differences are not remarkable for the normal-mass hierarchy. It is important to point out that 1D models overestimate the progenitor and neutrino oscillation dependence of the event rate for all detectors. The former trend is mainly due to the diminished accretion power in 3D models at later post-bounce times. The latter is mainly due to effects of PNS convection, for which the increase

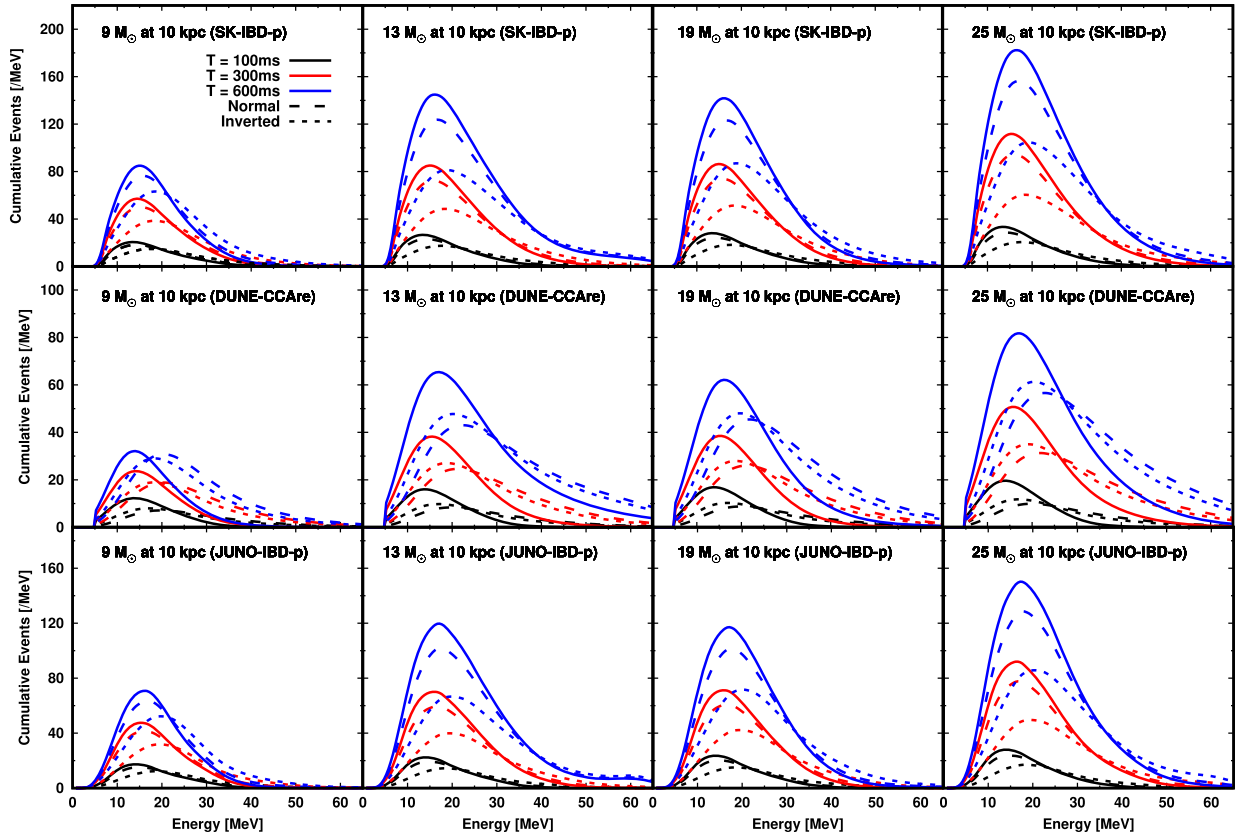radius in the 3D model is slightly larger than that in 1D, which reduces the efficiency of shock acceleration.

Figure 6. Energy spectrum of time-integrated (cumulative) event counts at three selected times, $T = 100$ (black), 300 (red), and 600 ms (blue), in the major detection channel for each detector (from top to bottom, SK, DUNE, and JUNO) boasting neutrino energy sensitivity and for selected progenitors (from left to right, 9-, 13-, 19-, and 25-$M_\odot$). Colour denotes the time and the line type distinguishes the neutrino oscillation model. The event total is angle averaged and the distance to the CCSN source is assumed to be 10 kpc.

in the ν_x luminosity and the decrease in the average energy of ν_e and $\bar{\nu}_e$ neutrinos reduce the flavour dependence of the event rate in all detectors. We find that the variation due to different oscillation models for a common 3D CCSN model is within a factor of $\sim$1.5 through the end of our simulations.

In Fig. 6, we provide energy spectra for the cumulative total number of events for the major channel of each detector for three selected post-bounce times: $T = 100$, 300, and 500 ms. We selected four representative 3D models. In computing these spectra, we took into account the smearing effects described in SNOWGLOBES. Regardless of progenitor, detector, or neutrino oscillation model, the peak of each energy spectrum increases with time and is located between $\sim$15 and $\sim$20 MeV. The overall shapes of the energy spectra are very similar for different progenitors, except for the 9-$M_\odot$ model. This difference is due to the early lack of an accretion component of the neutrino emission, which reduces not only luminosities, but also the average energy of the neutrinos (see Fig. 3). Furthermore, we find that the spectra become stiff once flavour conversion is taken into account. This is attributed to the fact that both ν_e and $\bar{\nu}_e$ spectra at the Earth are affected by ν_x (and $\bar{\nu}_x$) neutrinos at the CCSN source. It should be noted, however, that the total neutrino count in an energy bin decreases with increasing energy ($\gtrsim$30 MeV), This implies that the signal-to-noise ratio (SN ratio) is smaller for the high-energy tail and that it would be challenging to measure it. Thus, it would be better to study a different reaction channel with a higher sensitivity to high-energy neutrinos. Addressing the issue is beyond the scope of this paper.

3.2 Asymmetry of neutrino signals

It has been observed in multidimensional CCSN simulations that various mechanisms cause asymmetric neutrino emission (see e.g. O'Connor & Couch 2018; Walk et al. 2018; Glas et al. 2019; Harada et al. 2019; Nagakura, Sumiyoshi & Yamada 2019b; Vartanyan et al. 2019; Walk et al. 2019). This implies that the neutrino event rates depend on the angular location of the observer. Therefore, it is necessary to quantify the magnitude of such variations in the event rates at detectors. In this section, we quantify this quantity for our 3D CCSN models.

In our CCSN simulations, we employ 128×256 ($\theta \times \phi$) angular grid points; hence, we can in principle compute the neutrino event rate in each angular direction. However, those computations are very expensive and we are less interested in the results at a specific angular point, but rather in the global characteristics. For this purpose, we perform a spherical harmonic decomposition of the neutrino data obtained from our CCSN simulations. In each energy bin of the first moment of the neutrinos, we carry out the spherical harmonics decomposition by following equations (1)–(3) in Burrows, Dolence & Murphy (2012). We then compute the neutrino event rate by using SNOWGLOBES for each spherical harmonic coefficient, and then merge the results up to $\ell = 2$, taking into account the azimuthal dependence. Although this approach may discard fine angular structure of the neutrino signal, those structures are very sensitive to the realization of our numerical CCSN models. This indicates that statistical analyses with many realizations are required to study the fine structure, which is beyond the scope of this paper.
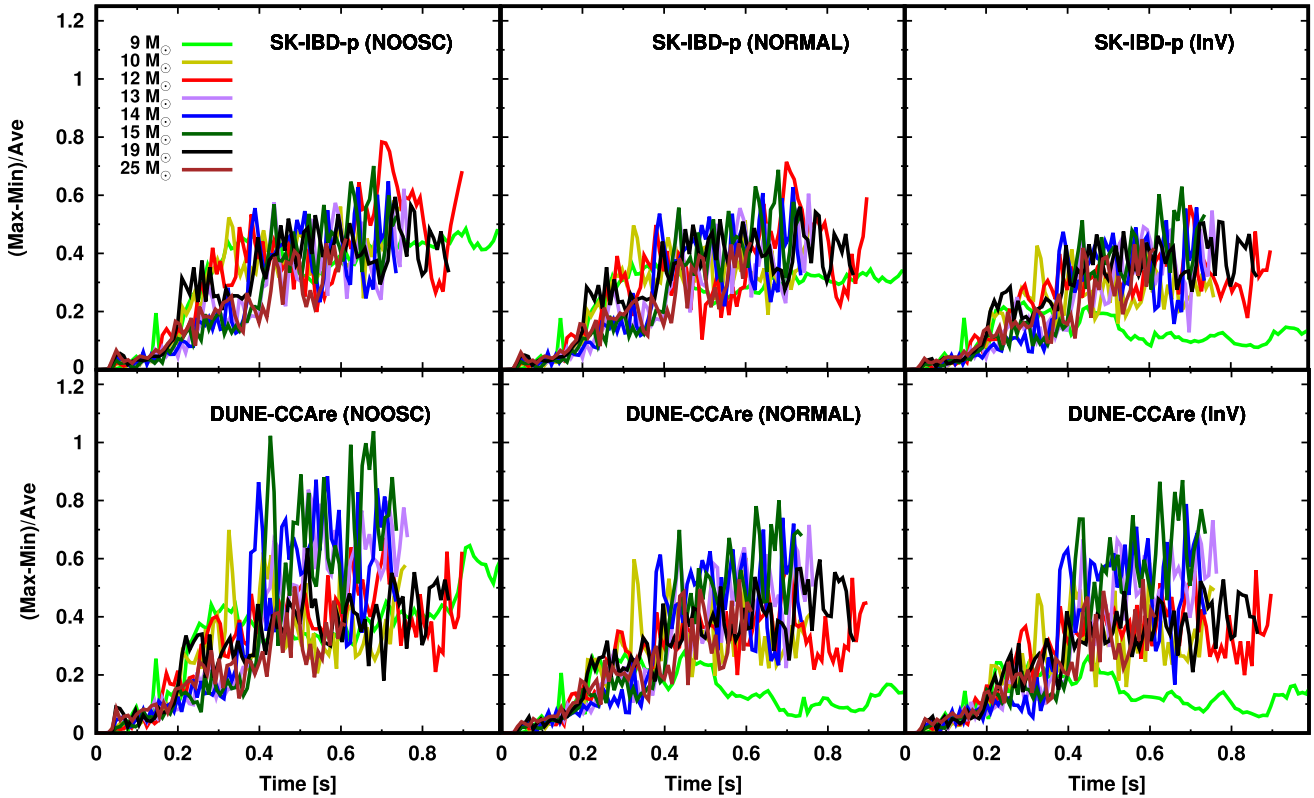
Figure 7. Angular variation of the neutrino event rate at SK (top) and DUNE (bottom) as a function of time. The asymmetry is measured by the difference between maximum and minimum event rates normalized by the angle-averaged one. Colour distinguishes CCSN models with different progenitor masses.

Nevertheless, our analysis captures the overall trends of the angular distributions of the neutrino event rates.

Fig. 7 portrays the angular asymmetry in the neutrino detection rate at SK and DUNE as a function of time. Since they are almost the same as in the case of SK, we omit the corresponding JUNO and IceCube plots. We define the degree of asymmetry as the difference between the maximum and minimum of the neutrino event rate, normalized by the angular average. Roughly speaking, the degree of asymmetry increases with time, except in the case of the 9-$M_\odot$ progenitor in both neutrino oscillation models. This exception is attributed to a combination of effects; (1) the earlier lack of an accretion component reduces the contribution of $\bar{\nu}_e$ neutrinos to the signal, implying that the ν_x neutrino contribution is greater in the 9-$M_\odot$ model, and (2) ν_x neutrino emissions are less asymmetric than other species (this trend is common for other CCSN models as well). As a result of these two effects, the asymmetry of the neutrino event rate is smaller.

For other progenitors, the degree of asymmetry exceeds ~ 50 per cent for SK. Meanwhile, it reaches ~ 100 per cent for DUNE (see Fig. 7). As shown in this figure, the strong asymmetry in DUNE is observed only for non-exploding models (13-, 14-, and 15-$M_\odot$), indicating that this is associated with the spiral SASI. As pointed out by Iwakami, Nagakura & Yamada (2014), the spiral SASI tends to emerge when the stalled shock wave is located at smaller radii ($\lesssim 100$ km), which is realized in our non-exploding models (Burrows et al. 2020). Our result also suggests that ν_e neutrino emissions at the source have the highest asymmetry, which also reflects the impact of the spiral SASI (see also Vartanyan et al. 2019). The spiral SASI effect is prominent in the vicinity of the shock wave, which affects the accretion component for ν_e neutrinos substantially. Although $\bar{\nu}_e$ neutrinos are also influenced by the spiral

SASI, their corresponding neutrinospheres are located at smaller radii than those for ν_e neutrinos, indicating that the impact of the spiral SASI for them becomes modest. We also find that the degree of asymmetry for neutrino oscillation models tends to be smaller than that for models with no flavour conversions, and this is due to the less asymmetric emissions of ν_x (and $\bar{\nu}_x$) neutrinos at the source.

Although there is a strong angular dependence in the instantaneous neutrino event rates, the angular asymmetry in the time-integrated count numbers tends to be more modest. Indeed, the asymmetry in the cumulative number of events is less than ~ 20 per cent among all our models (see Fig. 8). We also see a progenitor dependence in the difference between the event rate and the cumulative number of events. For non-exploding models, the asymmetry in the cumulative number of events is substantially reduced by integrating over time. This is attributed to the fact that the asymmetric neutrino emissions induced by the motions of the spiral SASI partially average out, smoothing the angular profile. On the other hand, the asymmetry of the 9-$M_\odot$ model behaves in an opposite way to that of the non-exploding models. As already pointed out, the asymmetry of this event rate is the smallest among our models, though the cumulative number of events is comparable to that for other models. This is attributed to the fact that the asymmetric neutrino emission in the 9-$M_\odot$ model seems to be mainly associated with the LESA, in which anticorrelated asymmetry between ν_e and $\bar{\nu}_e$ neutrino emissions appears coherently. Because of this coherency, the angular distribution of the cumulative number of events is not smoothed by the time integration, but rather accumulates with time. The asymmetric neutrino emissions of the 12-$M_\odot$ model are also associated with the LESA (see e.g. Vartanyan et al. 2019). Hence, this model has the highest asymmetry in the cumulative number of events among our models.
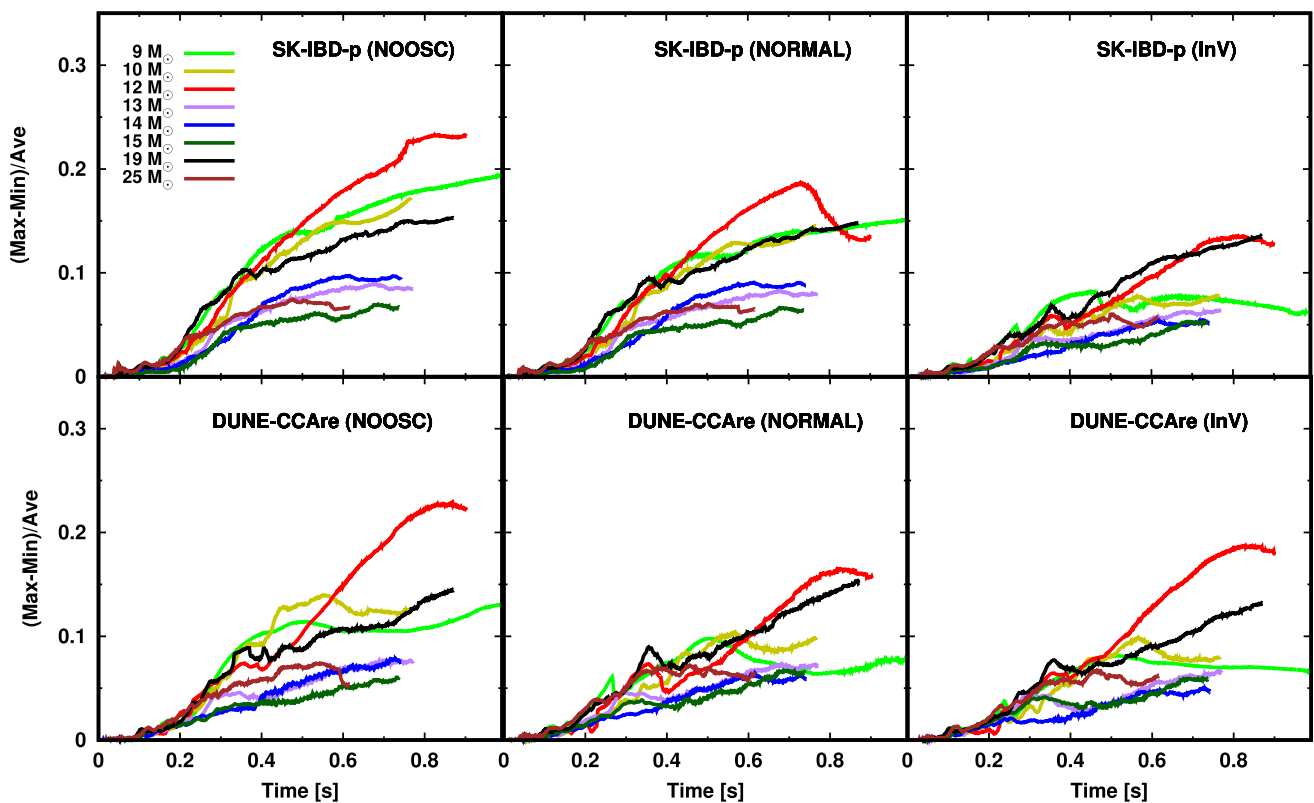
Figure 8. Same as Fig. 7, but for the time-integrated (cumulative) event rate.

Fig. 9 portrays the time evolution of cumulative number of events including its angular dependence. The shaded region corresponds to the range of the angular variations. We find that the angular variation is not large enough to smear out the progenitor dependence, implying that we may be able to place constraints on CCSN progenitors from the time evolution of the cumulative number of events. We also note that the uncertainty in the angular variations is comparable to the anticipated Poisson noise over a time integration with a window of ∼20 ms, assuming that the source distance is at 10 kpc. This indicates that Poisson noise does not compromise the constraint on the progenitor star mass using the time evolution of the cumulative number of events for $T \gtrsim 100$ ms.

3.3 Time variability due to the spiral SASI

As discussed above, the spiral SASI commonly occurs in non-exploding models (13-, 14-, and 15-M⊙) and this is a qualitatively distinct characteristic from the exploding models. In this section, we discuss the temporal behaviour of the neutrino signals in more detail.

In Fig. 10, we show the Fourier transform of the neutrino event rate in each detector. In the computation, we apply a Hann window function to the event rate during the time from core bounce to the end of each simulation. We also subtract the angle-averaged event rate to clearly see the spiral SASI feature.[6] Note also that we chose 24 sightlines and then take the average over the spectra. As shown in these plots, the temporal behaviour of the spiral SASI is clearly encoded in the neutrino signals; a strong peak can be seen

at $f \sim 100$ Hz (f denotes the frequency) and a modest peak is also observed at $f \sim 200$ Hz in all detectors. We also find that the peak is weaker in neutrino oscillation models than in the case with no flavour conversions, and we attribute this to the fact that ν_x neutrinos are less sensitive to the spiral SASI than ν_e and $\bar{\nu}_e$ neutrinos. This is consistent with the findings in our previous paper (Vartanyan et al. 2019).

However, it is challenging to resolve the temporal behaviour of the spiral SASI in neutrino signals. Below, we describe the degree of difficulty and discuss what is necessary to resolve it in each detector. We define α as a ratio of the neutrino energy associated with the spiral SASI (corresponding to the region around $f \sim 100$ Hz in our models) to the total emitted energy. According to previous studies (see also Lund et al. 2012; Tamborra et al. 2013; Walk et al. 2018; Vartanyan et al. 2019), α is roughly a few per cent or less. Thus, we set $\alpha = 10^{-2}$ as a representative value. We also define another variable, ΔT_{SASI}, which denotes the duration of the spiral SASI. Although it depends on progenitor model, we set $\Delta T_{SASI} = 500$ ms as a typical value. By using these values, we can estimate a number of neutrino events (N_{signal}) associated with the spiral SASI for a duration of $1/f$:

$$N_{signal} = 2 \left(\frac{N_{10\,kpc}}{10^4} \right) \left(\frac{\alpha}{0.01} \right) \left(\frac{f}{100\,Hz} \right)^{-1}$$
$$\times \left(\frac{\Delta T_{SASI}}{500\,ms} \right)^{-1} \left(\frac{d}{10\,kpc} \right)^{-2}, \qquad (20)$$

where $N_{10\,kpc}$ denotes the expected number of events if the source is located at 10 kpc; $N_{10\,kpc} = 10^4$ corresponds to the case with SK. We can estimate the Poisson noise of the event over the corresponding

---

[6]Note that the angle-averaged neutrino luminosity in our 3D models artificially fluctuates due to grid noises, which smears the SASI feature in the Fourier spectrum.
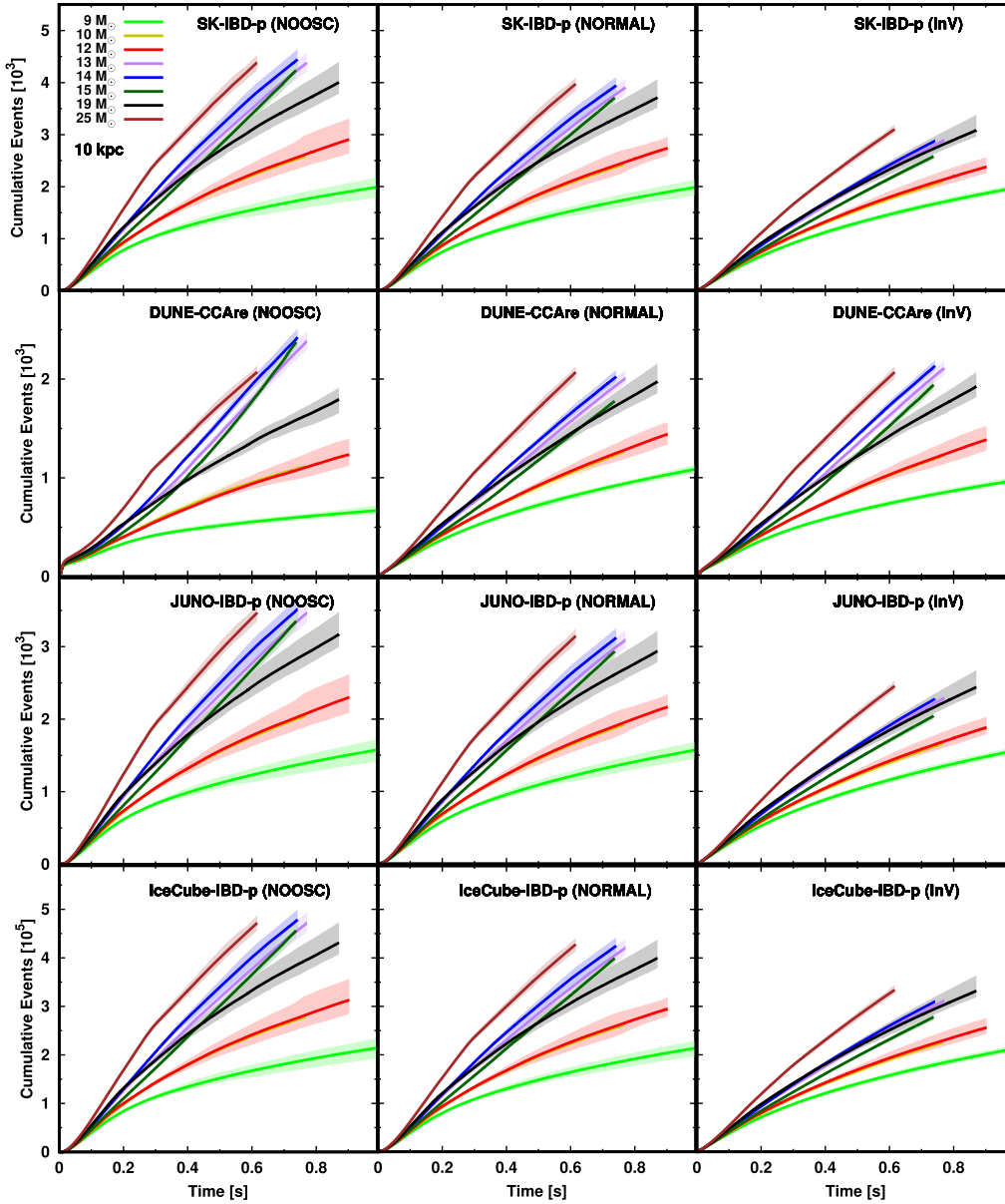
Figure 9. Time evolution of the cumulative number of events in the major channel of each detector (from top to bottom, SK, DUNE, JUNO, and IceCube). Left: no flavour conversions. Middle: normal-mass hierarchy. Right: inverted-mass hierarchy. Colour distinguishes the 3D models. The angular variations are also displayed with the shaded region along each solid line and the solid line corresponds to the angular average. The distance to the CCSN is assumed to be 10 kpc.

duration, $1/f$:

$$N_{\mathrm{noise}} = 5 \left(\frac{N_{10\,\mathrm{kpc}}}{10^4} \right)^{0.5} \left(\frac{f}{100\,\mathrm{Hz}} \right)^{-0.5}$$

$$\times \left(\frac{\Delta T}{4\,\mathrm{s}} \right)^{-0.5} \left(\frac{d}{10\,\mathrm{kpc}} \right)^{-1}, \qquad (21)$$

where ΔT corresponds to the time-scale of the overall neutrino emissions. We set $\Delta T = 4$ s as an example. As can be seen in these equations, the Poisson noise dominates the signal for SK if the CCSN is located at 10 kpc.[7] If we require that the SN ratio is larger

than 5, then the source should be located very nearby ($d \lesssim 1$ kpc). For HK, the threshold distance for HK is still ∼2 kpc.[8]

However, Tamborra et al. (2013) claim that HK is capable of detecting the temporal variation of the SASI in CCSNe at $d \geq 10$ kpc. There are some reasons for this inconsistency. First, those authors assume that the available volume in HK is 740 ktons, which is more than three times larger than that we assume. Secondly, their conclusion hinges on the choice of the most optimal observer direction in which the SASI modulation is strongest. Our conclusions rest on the use of the angle-averaged modulations, so their choice enhances the detectability of the temporal modulation in HK. We also

---

[7]We can estimate the signal and noise for DUNE and JUNO using equation (21) by changing $N_{10\,\mathrm{kpc}}$. Note that we arrive at a similar conclusion.

[8]We assume a fiducial volume of 220 ktons in HK for CCSN neutrino analysis (Hyper-Kamiokande Proto-Collaboration 2018).
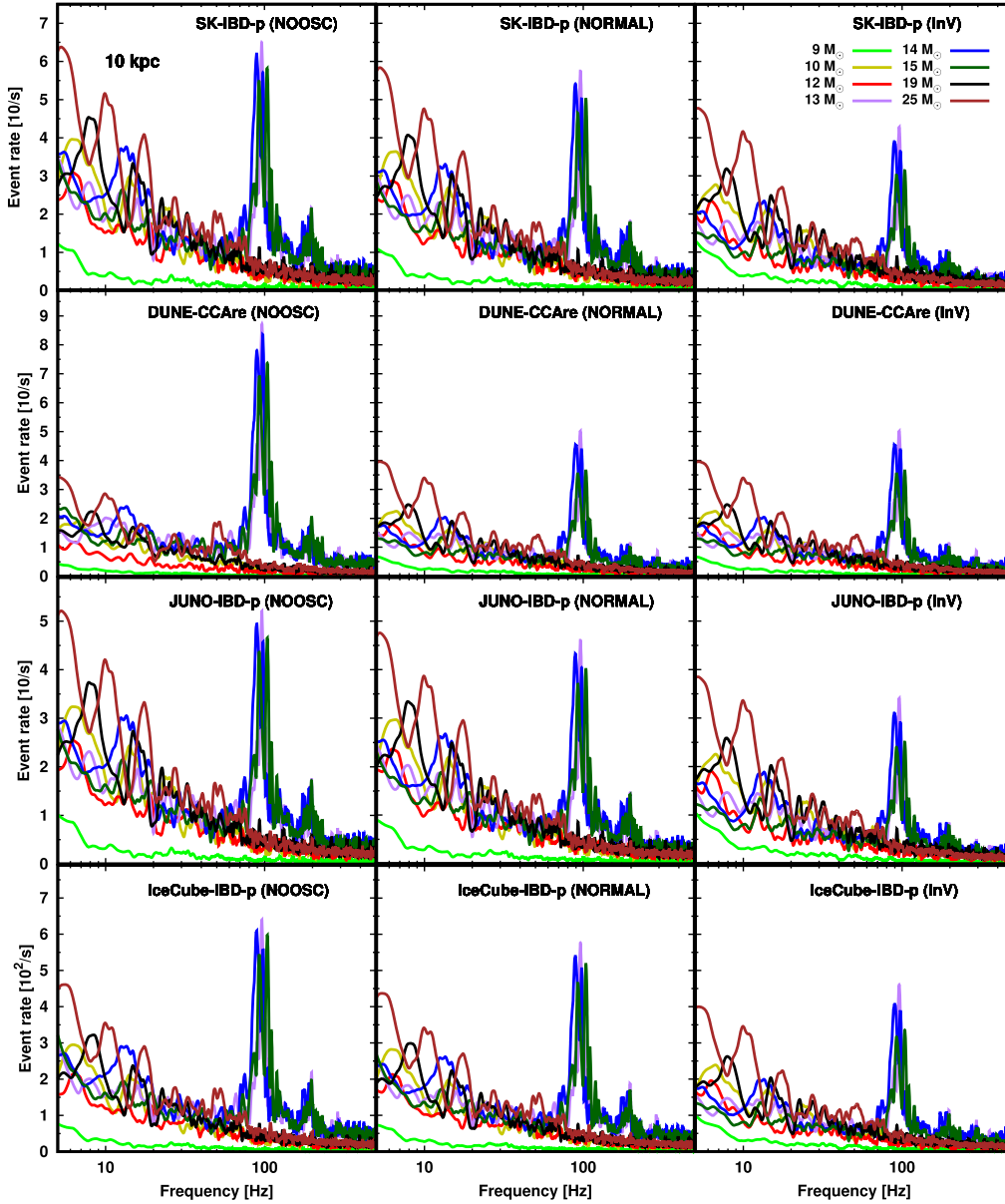
Figure 10. The finite-time Fourier transform of the neutrino event rate in each detector (from top to bottom, SK, DUNE, JUNO, and IceCube). Left: no flavour conversions. Middle: normal-mass hierarchy. Right: inverted-mass hierarchy. Colour distinguishes the 3D models. The distance to the CCSN source is assumed to be 10 kpc. A remarkable sharp peak at ∼100 Hz, which corresponds to the temporal behaviour induced by the spiral SASI, is seen, but only for non-exploding models. See the text for details.

note that in their analysis the SN ratio required to catch the temporal behaviour seems to be smaller than ours. They might be setting ∼2 (see the bottom panel of fig. 1 in Tamborra et al. 2013). Since the SN ratio is proportional to d^{-1}, the threshold distance becomes 2.5 times larger than ours by the difference in the SN ratio required for detection. As such, their conclusions are based on optimistic choices, and this accounts almost completely for the different conclusions.

For IceCube, on the other hand, the expected number of events is two orders of magnitude larger than that in SK, suggesting that it may be the most promising neutrino detector for investigating the temporal behaviour due to the spiral SASI (see also Tamborra et al. 2013; Walk et al. 2018). However, as mentioned, the noise characteristics of IceCube are different from those in other detectors, and this should be taken into account in the discussion of detectability. Here, we consider this following Tamborra et al. (2013).

From equation (20), we obtain $N_{\text{signal}} = 200$ for a CCSN at a distance of $d = 10$ kpc.[9] On the other hand, the background noise can be estimated as $1.48 \times 10^6 \times (1/100) = 1.48 \times 10^4$, implying that it is significantly larger than N_{signal}. However, the background noise is nearly in steady state. Hence, its time-averaged value can be subtracted. After the subtraction of the time-averaged component, the residual noise is the Poisson noise of the background and CCSN signals, estimated as

$$N_{\text{noise(IC)}} = \left(\frac{1.48 \times 10^6}{f} + \frac{N_{10\,\text{kpc}}}{\Delta T f} \left(\frac{d}{10\,\text{kpc}} \right)^{-2} \right)^{0.5}, \quad (22)$$

[9]In our simulations, we find that N_{signal} is ∼500 (see the bottom panels of Fig. 10), which is consistent to a factor of 2 with our rough estimate.

which yields $N_{noise(IC)} \sim 130$ for $\Delta T = 4$ s and $d = 10$ kpc, indicating an SN ratio of ~ 2. We note that our 3D models have an ~ 2.5 times higher signal than the rough estimation, indicating that the SN ratio is ~ 5.[10] Thus, our results suggest that the temporal behaviour of the spiral SASI at 10 kpc may be seen in the neutrino IceCube signal, albeit with low statistics. We note that, if the CCSN source distance is $d \lesssim 3$ kpc, the temporal fluctuation of the noise is dominated by the Poisson noise of the CCSN neutrinos (not the background), indicating that equation (21) becomes a good approximation to equation (22). The SN ratio becomes $\gtrsim 10$ at a distance of $d \lesssim 3$ kpc. Thus, we conclude that IceCube is currently the best detector with which to study the temporal behaviour of the spiral SASI, a conclusion consistent with the results of previous studies (Tamborra et al. 2013; Lin et al. 2020).

3.4 Correlations

Once we actually capture neutrino signals from CCSNe, we will attempt to estimate the total emitted energy of the neutrinos. This is directly related to the neutron star binding energy, a function of the residue mass and nuclear EOS. The most straightforward approach is to reconstruct the energy spectra for all flavours of neutrino at the Earth and then to compute the total radiated energy, taking into account the distance to the CCSN. As we shall see in Section 3.5, it is possible to use the data from multiple detectors to optimize the scientific return. However, the accuracy of the spectrum reconstruction depends on the SN ratio of the neutrino signal and a reliable estimation is possible only if the source is nearby. A major limitation in this process is also due to the estimates for heavy lepton neutrinos, detected only through reaction channels with moderate sensitivity. As a result, Poisson noise smears the energy spectra and induces large errors in estimates of the total radiated neutrino energy.

In this section, we consider this problem from a different angle, in which we incorporate the results of theoretical models in the analysis. More specifically, we look for theoretical correlations between observed quantities (e.g. the number of events at each detector) and the total neutrino energy (TONE) based on our 3D models. Although this approach is affected by uncertainties in the input physics in our CCSN models, it can be compared with the estimations based on direct spectrum reconstructions from observed data. We, hence, propose this method to combine with theoretical models as a complementary method to those based on purely observed quantities. It should also be emphasized that this approach can be very powerful, in particular for the analyses of CCSNe at great distances, since we would need only the energy- and time-integrated total event numbers in the major detection channel for each detector.

In advance of delving into the analysis, we mention an important point. In the previous sections, we revealed that the neutrino signals have a rich diversity across the progenitor continuum. Indeed, the time evolution of both event rate (see Fig. 4) and cumulative event number (see Fig. 9) strongly depends on the progenitor. This could be a major obstacle to our proposed method, since we do not know a priori the CCSN progenitor. Hence, it might be necessary to find correlations that are less sensitive to the progenitor.[11]

Similar to Fig. 9, we provide the cumulative number of events at each detector in Fig. 11, but as a function of TONE. Note that the TONE monotonically increases with time; thus, the map between time and TONE is monotonic for each model. For neutrino oscillation models, we find that TONE is less sensitive to progenitor. We also find that the uncertainty due to the progenitor dependence is comparable to that of the angular dependence (shaded region), i.e. the error is within a few tens of per cent. Hence, we conclude that the correlation is nearly universal (with little progenitor dependence). We emphasize that such universality is not trivial, since the reaction channels used in this study are not sensitive to heavy lepton neutrinos at the Earth. Nevertheless, our result suggests that the cumulative number of events in each reaction channel is universally correlated with the TONE.

As shown in Fig. 11, the progenitor dependence of the correlation is weaker for neutrino oscillation models vis-à-vis the no-oscillation models. One of the reasons is that the total radiated energy of the four heavy lepton neutrinos (ν_μ, ν_τ, and their antipartners) constitutes the dominant contribution to the TONE, although the individual contributions are smaller than those for the ν_e and $\bar{\nu}_e$ neutrinos.[12] This fact indicates that ν_x neutrinos at the source contain the most important information concerning the radiated total energy. For no-oscillation models, however, the observed data in the major reaction channels for each detector do not reflect ν_x neutrino properties at all, and as a result they tend to be less sensitive to the total energy. It should be mentioned that the ratio of the emitted energy of ν_e or $\bar{\nu}_e$ neutrinos to ν_x neutrinos varies with progenitor[13] (see also Fig. 3). This results in a large progenitor dependence in the correlation. For oscillation models, on the other hand, the observed data reflect some characteristics of ν_x neutrino emission at the source, and the degree of correlation depends upon the survival probability of the neutrinos. For the normal-mass hierarchy, ν_x neutrinos at the source turn into ν_e neutrinos at the Earth almost completely, indicating that DUNE would provide the most sensitive data with which to measure the TONE. For the inverted-mass hierarchy, $\bar{\nu}_x$ neutrinos at the source change into $\bar{\nu}_e$ neutrinos at the Earth, indicating that the observed data via the IBD-p reaction channel in SK, JUNO, and IceCube have the most direct correlation with the TONE, all of which is consistent with the results displayed in Fig. 11.

For convenience, we provide approximate formulae for the correlation in the case of the neutrino oscillation models. We fit the relation to quadratic functions. The fitting formulae are given in the case of normal-mass hierarchy as

$$[SK - IBDp - NORMAL]$$

$$N_{Cum} = \left(220\, E_{52} + 5\, E_{52}^2\right) \left(\frac{V}{32.5\,\text{ktons}}\right) \left(\frac{d}{10\,\text{kpc}}\right)^{-2}, \quad (23)$$

$$[DUNE - CCAre - NORMAL]$$

$$N_{Cum} = \left(90\, E_{52} + 4.5\, E_{52}^2\right) \left(\frac{V}{40\,\text{ktons}}\right) \left(\frac{d}{10\,\text{kpc}}\right)^{-2}, \quad (24)$$

---

[10]Note that the background noise is dominant at $d = 10$ kpc. Hence, the SN ratio is roughly proportional to the signal.

[11]However, a galactic supernova will be a target of a vast array of telescopes and the progenitor star, its mass, and distance are likely to be strongly constrained using photon observations.

[12]This is mainly due to the absence of charged-current reactions for heavy lepton neutrinos in supernova matter.

[13]This is due to the fact that the accretion component of the neutrino luminosity, which is the dominant contribution in ν_e and $\bar{\nu}_e$ emission, varies with different progenitor models.
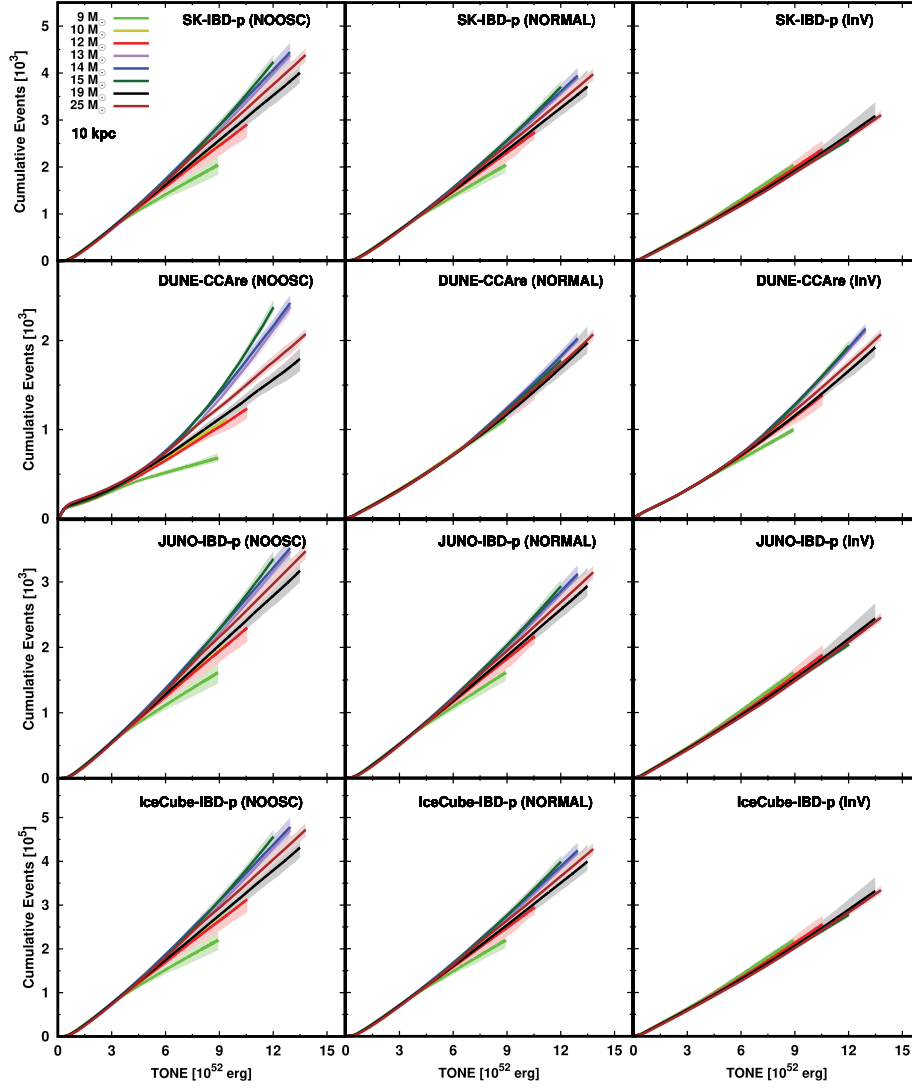
Figure 11. Same as Fig. 9, but as a function of the TONE.

[JUNO − IBDp − NORMAL]

$$N_{\rm Cum} = \left(165\,E_{52} + 4.5\,E_{52}^2\right)\left(\frac{V}{20\,{\rm ktons}}\right)\left(\frac{d}{10\,{\rm kpc}}\right)^{-2}, \quad (25)$$

[IceCube − IBDp − NORMAL]

$$N_{\rm Cum} = \left(23000\,E_{52} + 600\,E_{52}^2\right)\left(\frac{V}{3.5\,{\rm Mtons}}\right)\left(\frac{d}{10\,{\rm kpc}}\right)^{-2}, \quad (26)$$

and in the case with inverted-mass hierarchy as

[SK − IBDp − InV]

$$N_{\rm Cum} = \left(170\,E_{52} + 4\,E_{52}^2\right)\left(\frac{V}{32.5\,{\rm ktons}}\right)\left(\frac{d}{10\,{\rm kpc}}\right)^{-2}, \quad (27)$$

[DUNE − CCAre − InV]

$$N_{\rm Cum} = \left(90\,E_{52} + 4.5\,E_{52}^2\right)\left(\frac{V}{40\,{\rm ktons}}\right)\left(\frac{d}{10\,{\rm kpc}}\right)^{-2}, \quad (28)$$

[JUNO − IBDp − InV]

$$N_{\rm Cum} = \left(135\,E_{52} + 3\,E_{52}^2\right)\left(\frac{V}{20\,{\rm ktons}}\right)\left(\frac{d}{10\,{\rm kpc}}\right)^{-2}, \quad (29)$$

[IceCube − IBDp − InV]

$$N_{\rm Cum} = \left(18000\,E_{52} + 430\,E_{52}^2\right)\left(\frac{V}{3.5\,{\rm Mtons}}\right)\left(\frac{d}{10\,{\rm kpc}}\right)^{-2}, \quad (30)$$

where $N_{\rm Cum}$, E_{52}, and V denote the cumulative number of events, TONE in the unit of 10^{52} erg, and the detector volume, respectively. We note that equations (23) and (27) with $V = 220$ ktons provide the correlation for HK.

Although those formulae are useful to measure the TONE from $N_{\rm Cum}$, we need to mention two important points. First, those fits may be valid only for neutrino signals up to ∼1 s from its first event, since our simulations do not cover the later phases. Thus, the fitting formula may need to be corrected to cover the entire phase of a CCSN. We are currently extending some of our 3D simulations to include the longer term PNS cooling phase. Thus, we will address this issue in upcoming papers. Another important point is that the

fitting formulae are directly affected by theoretical uncertainties in our CCSN models. Although our simulations provide sophisticated representations of neutrino signals from CCSN, there remain several open issues with the input physics, implying that the formulae may need to be revised. Despite these limitations, equations (23)–(30) should be useful for estimating the TONE in real observations.

3.5 Retrieving neutrino spectra at CCSN sources

In the previous section, we showed that the cumulative number of events in each detector is capable of providing the TONE by means of a universal relation (correlation) that we found. As pointed out already, however, systematic errors are unavoidable with this approach due to uncertainties in the theoretical models. In addition to this, it is not easy to extract more detailed information on neutrino signals, such as the energy spectrum, which is accessible only by direct analyses with purely observed quantities.

Several methods have been proposed in the literature to reconstruct neutrino energy spectra from CCSNe. One of the common methods is by using an analytic formula, in which the spectrum is characterized by a combination of parameters. These parameters are estimated by taking statistical approaches that are very powerful for noisy data (see e.g. Minakata et al. 2008; Gallo Rosso, Vissani & Volpe 2017, 2018a; Gallo Rosso et al. 2018b). On the other hand, the spectrum reconstruction with analytic formula potentially discards some important characteristics of the signal, since the analytic formula is not capable of capturing the complex features of the spectrum. It should also be pointed out that the spectrum reconstruction of all neutrino flavours is a challenging issue even for next-generation detectors. Indeed, as already pointed out, detection techniques sensitive to heavy lepton neutrinos are still limited. Recently, Li et al. (2019) proposed an interesting strategy with liquid-scintillator detectors, in which they attempt to reconstruct the energy spectra of all the flavours by combining the data from three reaction channels: IBD-p, eES, and elastic scattering on protons. However, this technique has a large systematic error in the energy $\lesssim 20$ MeV, which corresponds to the most important energy range for CCSN neutrinos. This implies that other strategies are required to reconstruct the energy spectra more accurately.

We have tackled this issue and developed a novel technique for spectrum reconstruction, in which data on multiple channels at different detectors are combined. In this section, we apply our method to neutrino events computed by SNOWGLOBES based on our 3D CCSN models and retrieve energy spectra for all neutrino flavours at the CCSN source assuming that the distance is known. Note that the Poisson noise and smearing effects due to detector responses are taken into account in this demonstration to mimic real observations. We also evaluate how accurately one can estimate the average energy and total energy of neutrinos. Although this technique can still be improved, the proposed method is useful for determining how efficiently one can combine neutrino data from multiple detectors to retrieve the energy spectra of all neutrinos at the source. Below, we briefly review the essence of our method and then present the results. The details of the method are complex and should be described structurally; hence, we present them in another paper separately (Nagakura 2020).

In our method, the observed data at HK and DUNE, which have different flavour sensitivities, are adopted. Also, including HK is mandatory, unless the source is quite nearby $d \lesssim 0.5$ kpc, in which case the same method can be applied using SK and DUNE. Hence, we focus only on the use of HK and DUNE. For HK, we employ two reaction channels: IBD-p and eES. For DUNE, the CCAre channel is adopted. As we describe in Section 2.2, IBD-p and CCAre are sensitive to $\bar{\nu}_e$ and ν_e neutrinos, respectively. Note that these reaction channels provide most of the events in each detector, i.e. they are high statistics. For eES, on the other hand, the reaction channel is sensitive to all neutrino flavours, although the number of counts is much smaller than that via the IBD-p. It should be pointed out that we cannot easily discern the flavour-dependent eES events individually, since all events are detected through a common signal (Cherenkov light from scattered electrons).[14]

As mentioned above, three reaction channels with different flavour sensitivities are employed in our approach, which is a minimum required to retrieve the neutrino spectra of all neutrino flavours at the CCSN source. This is due to the fact that there are three independent spectra (ν_e, $\bar{\nu}_e$, and ν_x) under the assumption that the energy spectra of heavy lepton neutrinos and their antipartners are identical at the source.[15] We employ a singular value decomposition (SVD) technique (Höcker & Kartvelishvili 1996). This approach does not assume any a priori analytic formula for the spectrum shape, but evaluates the spectrum in a deterministic way. In addition, we develop an adaptive energy mesh technique with the SVD unfolding algorithm, in which the energy gridding is automatically adjusted in accordance with the energy-dependent events.

First, we apply the unfolding technique to the data for the IBD-p and CCAre, which provides us with the energy spectra of $\bar{\nu}_e$ and ν_e neutrinos in HK and DUNE, respectively. Based on these two energy spectra, we identify the eES events with ν_e and $\bar{\nu}_e$ neutrinos and then obtain the eES events of the heavy lepton neutrinos by subtracting the ν_e and $\bar{\nu}_e$ neutrino contributions from the total number of eES events.[16] It should be noted that we distinguish the spectra of ν_x and $\bar{\nu}_x$ neutrinos at the Earth, as described in Section 2.3, and doing so is mandatory in our method (since the eES cross-sections are different for neutrinos and antineutrinos). This indicates that we need to separate the eES events and this is possible using the assumption that

---

[14]Although the flavour-dependent events cannot be resolved in the eES channel, the IBD-p and eES events may be distinguished by virtue of their different angular distributions; the former is almost isotropic and the latter is forward-peaked. We also note that the addition of gadolinium greatly enhances the ability to separate these two channels. Hence, we assume in this study that we can completely distinguish the two channels. Note that we ignore the charged-current reactions with oxygen, since they are subdominant channels. However, it should be pointed out that in our method it is straightforward to add these channels.

[15]We note, however, that we may need to relax this assumption in real data analysis, since their neutrino–matter interactions in supernova matter are not exactly the same and the difference increases with increasing neutrino energy. As we will discuss in a forthcoming paper (Nagakura and Hotokezaka, in preparation), it is possible to distinguish them, although the strategy is different from that used in this paper.

[16]In general, the neutrino flavour state is not always the same for HK and DUNE, mainly due to the different Earth matter effects. This indicates that ν_e neutrinos at DUNE are different from those in HK (SK). Thus, one may wonder if this compromises the accuracy of the subtraction of the ν_e neutrino contribution of the eES events from the total. This is, however, not an obstacle in our method. Indeed, the Earth matter effects (and other neutrino oscillation models including non-adiabatic MSW effects and neutrino–neutrino self-interactions) can be treated self-consistently in our method. This is attributed to the fact that, again, the problem is to retrieve the three unknown energy spectra from the three independent observed data, which mathematically guarantees a unique solution. We refer readers to Nagakura (2020) for more details.
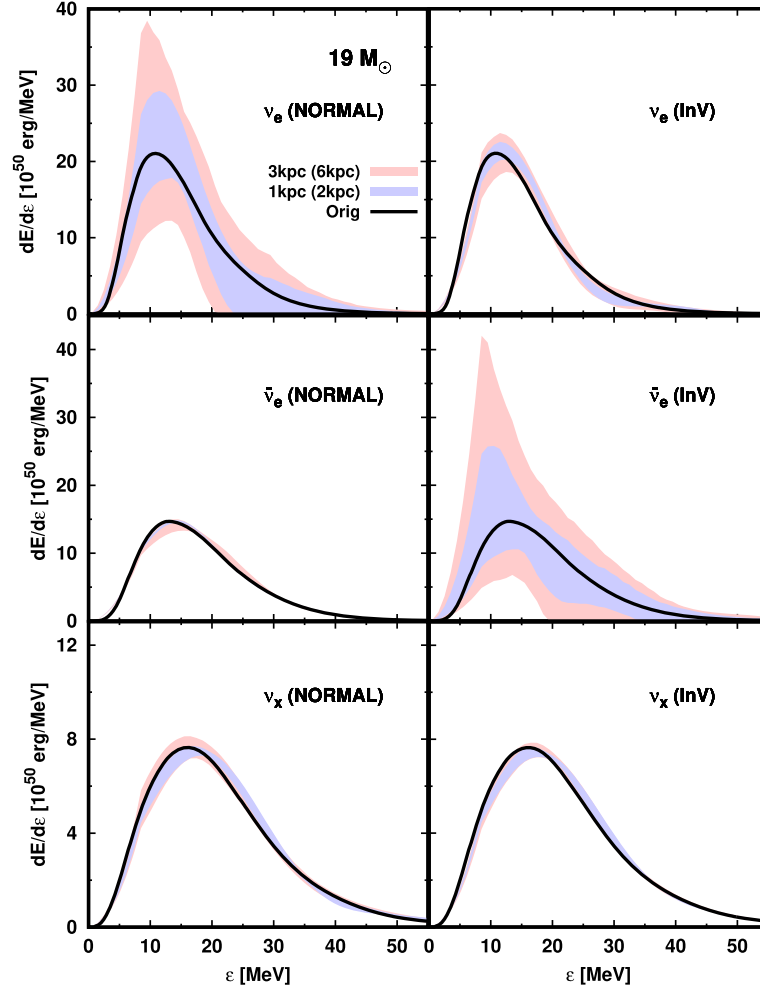
Figure 12. The time-integrated energy spectra for the 3D 19-$M_\odot$ model at the CCSN source retrieved by our method (see the text for more details). We focus on the data at $T = 0.871$ s, which corresponds to the time at the end of the simulation. From top to bottom, ν_e, $\bar{\nu}_e$, and ν_x neutrinos, respectively. The left- and right-hand panels show the results for the normal-mass hierarchy and inverted-mass hierarchy, respectively. The colour distinguishes the source distance. The solid black line corresponds to the solution of the spectrum (corresponding to the result for the CCSN simulation). The shaded region corresponds to the $\sim 2\sigma$ confidence level. The distance in parentheses denotes the corrected one including all phases of the CCSN. See the text for further details.

ν_x and $\bar{\nu}_x$ neutrinos have identical spectra at the CCSN source. This technique requires that we iteratively search for consistent spectra using this condition. Finally, we convert the energy spectra of all neutrino flavours at the Earth to those at the CCSN source by using equations (12)–(15) (and the source distance).

In Fig. 12, we show results of the spectrum reconstruction for the 3D 19-$M_\odot$ model. We apply our method to the energy spectrum of the cumulative number of events in each reaction channel at the end of our simulations ($T = 0.871$ s for the corresponding model). The distance to the source is set as $d = 3$ kpc or 1 kpc.[17] It should be observed that our simulations do not cover the later PNS cooling phase ($T \gtrsim 1$ s), implying that the TONE in our CCSN models is smaller than its final value. Indeed, the TONE of all our 3D CCSN models is $\sim 10^{53}$ erg, which is a factor of $\sim$3–4 smaller than the expected total emitted neutrino energy from CCSNe. This indicates that our method would be capable of providing reliable energy spectra for CCSNe with the same accuracy at roughly a factor of $\sim$2 greater distance when all phases are included. Therefore, we also indicate the

corrected distance as a reference in Fig. 12 (shown in the parentheses in the top left panel of the figure). In this demonstration, we perform the analysis with 1000 Poisson noise realizations for each model. The shaded region in Fig. 12 corresponds to the $\sim 2\sigma$ confidence level.

For the normal-mass hierarchy (left-hand panels in Fig. 12), energy spectra of $\bar{\nu}_e$ and ν_x neutrinos at the source are well retrieved. Most of the ν_x neutrinos at the source turn into ν_e neutrinos at the Earth, indicating that the spectrum reconstruction of ν_e neutrinos from CCAre events at DUNE is responsible for the ν_x neutrino spectrum at the source. By using IBD-p events in HK, we can reconstruct precisely the energy spectrum of $\bar{\nu}_e$ neutrinos at the Earth for which $\bar{\nu}_e$ and $\bar{\nu}_x$ neutrinos at the source are mixed (see equation 13). The high-precision energy spectrum of $\bar{\nu}_e$ neutrinos at the Earth (by IBD-p in HK) and that for $\bar{\nu}_x$ neutrinos at the source (using the assumption that $\bar{\nu}_x = \nu_x$ at the source, well retrieved by the CCAr data in DUNE) provide a precise $\bar{\nu}_e$ energy spectrum at the source. Incidentally, the above explanation makes clear that the IBD-p and CCAre channels in HK and DUNE, respectively, do not constrain ν_e neutrino spectra at the source; these are determined mainly through the eES channel. As shown in the figure, however, the error in the ν_e energy spectrum at the source is significantly larger than that for other species. There

---

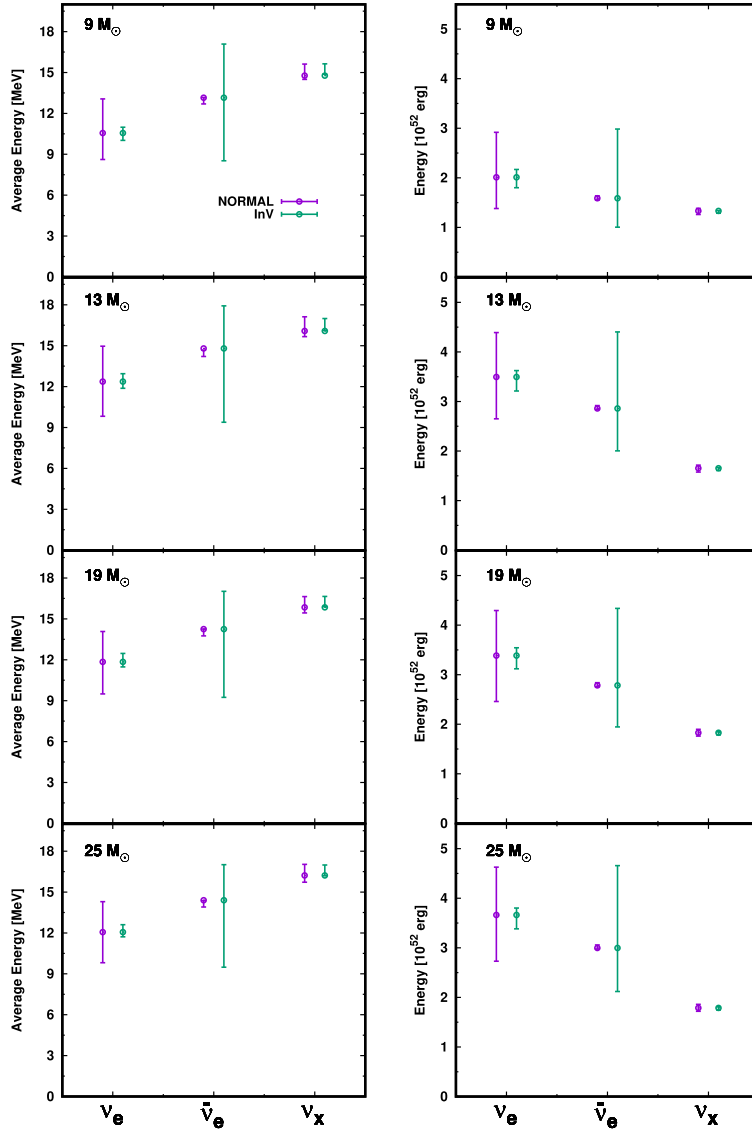[17]Note that the SN ratio is inversely proportional to the distance.

Figure 13. The average energy (left) and total energy (right) for each neutrino species retrieved by our spectrum reconstruction technique. The distance to the source is assumed to be 3(6) kpc. From top to bottom, we display the results for different 3D models: 9-, 13-, 19-, and 25-M$_\odot$. Purple and green colours denote the case with normal-mass hierarchy and inverted-mass hierarchy, respectively. The error bar corresponds to the $\sim 2\sigma$ confidence level, while the open circles correspond to results from our CCSN simulations.

are a few reasons for this lower precision. As already mentioned, the number of eES events is much smaller than that for IBD-p. Indeed, the SN ratio is several times smaller than that for the IBD-p. Furthermore, we reconstruct the energy spectrum of ν_x neutrinos at the Earth by employing a subtraction process for the eES events. As a result, the ν_x signal is smaller than that for the total eES contribution. Meanwhile, the noise is determined by the total number of eES events, implying that the SN ratio of eES events for ν_x neutrinos becomes smaller than that of the total. It should be mentioned that the cross-section for the eES reactions with ν_e and $\bar{\nu}_e$ neutrinos is higher than that for heavy lepton neutrinos. This is due to the fact that ν_e and $\bar{\nu}_e$ neutrinos interact with electrons through both charged-current and neutral-current reactions, while heavy lepton neutrinos react only through neutral currents.

In the case of the inverted-mass hierarchy, on the other hand, the energy spectra of ν_e and ν_x neutrinos can be precisely retrieved. The reason is very similar to the case for the normal hierarchy. $\bar{\nu}_x$

neutrinos at the source turn into $\bar{\nu}_e$ neutrinos almost completely. This indicates that the spectral reconstruction of $\bar{\nu}_e$ neutrinos through the IBD-p channel in HK is directly connected with the precise estimation of the energy spectrum of $\bar{\nu}_x$ neutrinos at the source. This also provides the energy spectrum of ν_x neutrinos at the source, implying that the ν_e neutrino spectrum at the source can be retrieved accurately by combining the energy spectrum of the ν_x neutrinos at the source and the ν_e neutrino spectrum at the Earth, reconstructed using the CCAre channel in DUNE. Following the same argument, the energy spectrum of $\bar{\nu}_e$ neutrinos at the source reflects the large statistical error of the spectral reconstruction of $\bar{\nu}_x$ neutrinos.

In Fig. 13, we show the results of the retrieval of the average energy and emitted total energy of each neutrino species at the source for selected models. In the analysis, the source distance is assumed at 3(6) kpc and the error bar corresponds to an $\sim 2\sigma$ confidence level. The precision of the reconstruction of the energy spectrum directly reflects the statistical uncertainty, in which the
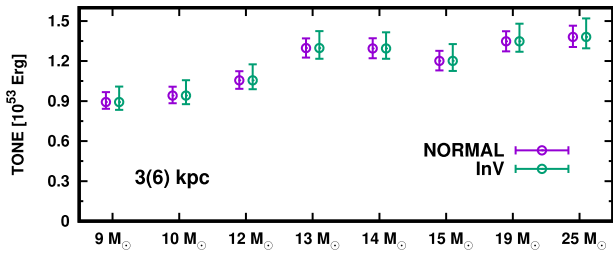
Figure 14. TONE estimated using energy spectra retrieved by our method. We show the results for all 3D models at the end of our simulations. Purple and green colours denote the normal-mass hierarchy and inverted-mass hierarchy, respectively. The error bar corresponds to the ∼2σ confidence level, and the open circles correspond to the results from CCSN simulations.

average energy and the emitted total energy of ν_e and $\bar{\nu}_e$ neutrinos are poorly retrieved for both the normal- and inverted-mass hierarchies, respectively. However, for other species in both oscillation models, the statistical uncertainties in both quantities are within ∼20 per cent (∼2σ confidence level).

As shown above, the precision of the reconstruction of the energy spectra, average energy, and total emitted energy depends upon both the flavour and oscillation model. ν_x neutrinos at the source can be well determined in both oscillation models. This is due to the fact that either p or $\bar{p}$ is close to zero for both oscillation models, implying that the reconstructed energy spectrum of $\bar{\nu}_e$ neutrinos (via IBD-p in HK) or ν_e neutrinos (via CCAre in DUNE) provides with high-precision energy spectrum of ν_x neutrinos at the source. This property is shared by other oscillation models, unless both p and $\bar{p}$ are above 0.5 (which corresponds to less realistic models with less flavour mixing).[18] This indicates that we will probably be able to retrieve the energy spectrum of ν_x neutrinos at the source for any realistic oscillation model. This aspect is an important advantage of estimating the TONE, since the four-species-integrated energy of ν_x neutrinos is the dominant contribution. Indeed, we confirm that the error in TONE is within ∼20 per cent (∼2σ confidence level) for all 3D models (see Fig. 14) if the source is located at 3(6) kpc.

Such a highly precise measurement of the TONE will enable the extraction of useful physical information for CCSNe. For instance, as shown in Fig. 9, the time evolution of the cumulative number of events at each detector has a strong progenitor dependence, since it varies by a factor of a few for the different progenitors. This indicates that we will be able to place constraints on the progenitor by applying our method to the cumulative number of events in each detector up to the post-bounce time of ∼1 s in real observations. Indeed, as shown in our previous studies (Burrows et al. 2019, 2020), CCSNe with lower mass progenitors tend to have lower total emitted neutrino energies, enabling the discrimination of different progenitor models using our method. It is important to remind the reader that the TONE estimated from the direct spectral reconstructions presented here can be compared with that estimated using the universal relation discussed in Section 3.4.

---

[18]There is no evidence that the Earth matter effect, non-adiabatic MSW effects, or neutrino–neutrino self-interactions, which are not taken into account in our analysis, substantially diminish the degree of flavour conversion for either neutrinos or antineutrinos. Hence, a small flavour conversion model seems unlikely.

4 SUMMARY AND CONCLUSIONS

Despite the theoretical determination that the fluid dynamics and neutrino transport in CCSN strongly depend upon dimension, most of the previous studies of the neutrino signal have involved 1D models. However, 3D models are clearly more realistic. This defect in previous work is due mainly to the fact that the much more computational expensive high-fidelity 3D models have only recently become available. These new 3D models exhibit a spectrum of behaviours, and most explode, indicating that 3D numerical models have made remarkable progress. Motivated by this development, we have performed the first systematic study of neutrino signals in terrestrial detectors for our 3D CCSN models with the aid of the SNOWGLOBES detector software. The results reveal some distinct differences with 1D models.

In this paper, we first illuminated the differences between 1D and 3D models in the neutrino event rates in each detector (see Fig. 4). PNS convection is the most important reason for the differences seen. As discussed in Section 2.1 (see also Nagakura et al. 2020), PNS convection lifts the ν_x neutrino luminosity, but decreases the average energy of the ν_e and $\bar{\nu}_e$ neutrinos compared with 1D models. The result is a systematic difference in the neutrino event rates. We found that there are interesting differences in the neutrino signals and signatures that distinguish non-exploding and exploding models, with an important role played by PNS convection. These ingredients are missing in previous studies based on 1D models.

In Section 3.2, we studied the angular (observer direction) dependence of the neutrino signal and quantified the angular variations. We found that the asymmetry of the angular distribution of the neutrino event rate can be quite large, reaching ∼100 per cent at some time snapshots in some models (see Fig. 7), though the angular variation in the cumulative total event number (see Fig. 8) might be more modest. The difference in the asymmetries of the event rate and cumulative number of event is remarkable, in particular for non-exploding models (13-, 14-, and 15-$M_\odot$ models). This can be understood through the properties of the spiral SASI, which appears only in our non-exploding 3D models. Its spiral motions introduce distinctive temporal modulation and large angular asymmetries in the neutrino signals. On the other hand, the angular asymmetry and its directionality vary somewhat randomly with time, indicating that the time-integrated signals (i.e. the cumulative number of events) are more isotropic. It should be noted, however, that the LESA is involved in most of our 3D models and it results in coherent asymmetric neutrino emission, implying that the time integration does not substantially reduce the asymmetry. Nevertheless, we find for all our 3D models that the angular variation of the cumulative number of events is ≲20 per cent up to the end of each simulation. It should be pointed out that the asymmetry in neutrino signals is smaller for neutrino oscillation models than that when ignoring flavour conversion. This reflects a property of ν_x neutrino emissions at the source, which are emitted more isotropically than other neutrino species.

In addition, we discussed the detectability of time variations induced by the spiral SASI encoded in neutrino signals by combining results of our simulations and semi-analytic estimates (see Section 3.3). We showed that the temporal behaviour can be resolved by SK, DUNE, and JUNO only if the source is located at ≲1 kpc. The threshold distance is extended to ∼2 kpc for HK. On the other hand, IceCube may be capable of resolving the temporal behaviour even when $d \sim 10$ kpc, albeit with low statistics (SN ratio is a few). We concluded that IceCube is the best detector for a temporal analysis of the spiral SASI and that the analysis of the temporal properties

of the neutrino signal will yield important insights into the internal dynamics of CCSNe.

We provided equations (23)–(30) to estimate the TONE from the cumulative number of events in each detector. This approach was designed to avail ourselves of correlations manifesting less of a progenitor dependence (see Section 3.4 for more details). Although there remain some uncertainties in our theoretical models, those correlations will prove useful for analysing real observations, and would be very powerful when analysing low-statistics neutrino signals, i.e. for distant CCSNe. We also developed a novel method by which to retrieve energy spectra for all neutrino flavours at the CCSN source based on purely observational quantities using multiple detectors, in particular HK (SK) and DUNE (see Section 3.5). The proposed method does not a priori assume any analytic formulae. We demonstrated that the energy spectrum of ν_x neutrinos and that of either ν_e or $\bar{\nu}_e$ neutrinos at the source can be retrieved using our new method (see Fig. 12). This indicates that the TONE can be estimated rather precisely, since the four-species-integrated energy of ν_x neutrinos is the dominant contribution to the total radiated energy. At a distance of $d = 3(6)$ kpc, we can estimate each to an accuracy of ∼20 per cent (Fig. 14) by using this method.

Finally, we provide several caveats. The largest is that our 3D CCSN simulations should be extended to cover the late-time PNS cooling phase ($\gtrsim 1$ s), during which more than half of the TONE is emitted. Theoretical predictions of the late-time evolution are necessary to determine whether the central remnant is a neutron star or black hole (for which case the signal abruptly ceases upon relativistic collapse; see e.g. Burrows 1986; Sumiyoshi et al. 2006), and its properties. Secondly, more detailed studies are called for of the sensitivities to the input physics in our CCSN models. For instance, we need to determine the nuclear equation-of-state dependence, as well as that of various neutrino–matter interactions. We leave these broad tasks to future work.

DATA AVAILABILITY

The data underlying this article will be shared on reasonable request to the corresponding author.

REFERENCES

Abbar S., 2020, J. Cosmol. Astropart. Phys., 2020, 027
Abbar S., Duan H., Sumiyoshi K., Takiwaki T., Volpe M. C., 2019, Phys. Rev. D, 100, 043004
Abbasi R. et al., 2011, A&A, 535, A109
Abe K. et al., 2016, Astropart. Phys., 81, 39
Acciarri R. et al., 2016, preprint (arXiv:1601.05471)
An F. et al., 2016, J. Phys. G Nucl. Phys., 43, 030401
Ankowski A. et al., 2016, preprint (arXiv:1608.07853)
Asakura K. et al., 2016, ApJ, 818, 91
Beacom J. F., Farr W. M., Vogel P., 2002, Phys. Rev. D, 66, 033001
Bhattacharyya S., Dasgupta B., 2020, Phys. Rev. D, 102, 063018
Bian J., 2015, preprint (arXiv:1509.07739)
Bionta R. M. et al., 1987, Phys. Rev. Lett., 58, 1494
Blondin J. M., Shaw S., 2007, ApJ, 656, 366
BOREXINO Collaboration, 2009, Nucl. Instrum. Methods Phys. Res. A, 600, 568
Burrows A., 1986, ApJ, 300, 488
Burrows A., Reddy S., Thompson T. A., 2006, Nucl. Phys. A, 777, 356
Burrows A., Dolence J. C., Murphy J. W., 2012, ApJ, 759, 5
Burrows A., Radice D., Vartanyan D., 2019, MNRAS, 485, 3153
Burrows A., Radice D., Vartanyan D., Nagakura H., Skinner M. A., Dolence J. C., 2020, MNRAS, 491, 2715
Capozzi F., Di Valentino E., Lisi E., Marrone A., Melchiorri A., Palazzo A., 2017, Phys. Rev. D, 95, 096014
Cross R., Fritz A., Griswold S., 2019, preprint (arXiv:1908.07249)
Delfan Azari M. et al., 2020, Phys. Rev. D, 101, 023018
Dighe A. S., Smirnov A. Y., 2000, Phys. Rev. D, 62, 033007
Gallo Rosso A., Vissani F., Volpe M. C., 2017, J. Cosmol. Astropart. Phys., 2017, 036
Gallo Rosso A., Vissani F., Volpe M. C., 2018a, J. Cosmol. Astropart. Phys., 2018, 040
Gallo Rosso A., Abbar S., Vissani F., Volpe M. C., 2018b, J. Cosmol. Astropart. Phys., 2018, 006
Glas R., Janka H. T., Melson T., Stockinger G., Just O., 2019, ApJ, 881, 36
Glas R., Janka H. T., Capozzi F., Sen M., Dasgupta B., Mirizzi A., Sigl G., 2020, Phys. Rev. D, 101, 063001
Halzen F., Jacobsen J. E., Zas E., 1996, Phys. Rev. D, 53, 7359
Harada A., Nagakura H., Iwakami W., Okawa H., Furusawa S., Matsufuru H., Sumiyoshi K., Yamada S., 2019, ApJ, 872, 181
Hirata K. et al., 1987, Phys. Rev. Lett., 58, 1490

Höcker A., Kartvelishvili V., 1996, Nucl. Instrum. Methods Phys. Res. A, 372, 469

Horowitz C. J., Caballero O. L., Lin Z., O'Connor E., Schwenk A., 2017, Phys. Rev. C, 95, 025801

Hüdepohl L., Müller B., Janka H. T., Marek A., Raffelt G. G., 2010, Phys. Rev. Lett., 104, 251101

Hyper-Kamiokande Proto-Collaboration, 2018, preprint (arXiv:1805.04163)

Iwakami W., Nagakura H., Yamada S., 2014, ApJ, 786, 118

Johns L., Nagakura H., Fuller G. M., Burrows A., 2020, Phys. Rev. D, 101, 043009

Köpke L., IceCube Collaboration, 2011, J. Phys. Conf. Ser., 309, 012029

Kuo T. K., Pantaleone J., 1989, Phys. Rev. D, 39, 1930

Langanke K., Martínez-Pinedo G., Müller B., Janka H. T., Marek A., Hix W. R., Juodagalvis A., Sampaio J. M., 2008, Phys. Rev. Lett., 100, 011101

Li H.-L., Huang X., Li Y.-F., Wen L.-J., Zhou S., 2019, Phys. Rev. D, 99, 123009

Lin Z., Lunardini C., Zanolin M., Kotake K., Richardson C., 2020, Phys. Rev. D, 101, 123028

Lunardini C., Smirnov A. Y., 2001, Nucl. Phys. B, 616, 307

Lund T., Wongwathanarat A., Janka H.-T., Müller E., Raffelt G., 2012, Phys. Rev. D, 86, 105031

Minakata H., Nunokawa H., Tomàs R., Valle J. W. F., 2008, J. Cosmol. Astropart. Phys., 2008, 006

Morinaga T., Nagakura H., Kato C., Yamada S., 2020, Phys. Rev. Res., 2, 012046

Müller B., 2019, Annu. Rev. Nucl. Part. Sci., 69, 253

Müller B., Janka H.-T., 2015, MNRAS, 448, 2141

Nagakura H., 2020, preprint (arXiv:2008.10082)

Nagakura H. et al., 2018, ApJ, 854, 136

Nagakura H., Burrows A., Radice D., Vartanyan D., 2019a, MNRAS, 490, 4622

Nagakura H., Sumiyoshi K., Yamada S., 2019b, ApJ, 880, L28

Nagakura H., Morinaga T., Kato C., Yamada S., 2019c, ApJ, 886, 139

Nagakura H., Burrows A., Radice D., Vartanyan D., 2020, MNRAS, 492, 5764

Nakazato K., Sumiyoshi K., Suzuki H., Totani T., Umeda H., Yamada S., 2013, ApJS, 205, 2

Nunez C., Scholberg K., Conley E., Deep Underground Neutrino Experiment Collaboration, 2017, APS Division Nuclear Physics Hawaii Meeting 2017, abstract id. EA.119

O'Connor E. P., Couch S. M., 2018, ApJ, 865, 81

O'Connor E., Ott C. D., 2013, ApJ, 762, 126

Pryor C., Roos C. E., Webster M. S., 1988, ApJ, 329, 335

Radice D., Burrows A., Vartanyan D., Skinner M. A., Dolence J. C., 2017, ApJ, 850, 43

Rampp M., Janka H.-T., 2002, A&A, 396, 361

Roberts L. F., Shen G., Cirigliano V., Pons J. A., Reddy S., Woosley S. E., 2012, Phys. Rev. Lett., 108, 061103

Scholberg K., 2012, Annu. Rev. Nucl. Part. Sci., 62, 81

Seadrow S., Burrows A., Vartanyan D., Radice D., Skinner M. A., 2018, MNRAS, 480, 4710

Shalgar S., Tamborra I., 2019, ApJ, 883, 80

Simpson C. et al., 2019, ApJ, 885, 133

Skinner M. A., Burrows A., Dolence J. C., 2016, ApJ, 831, 81

Skinner M. A., Dolence J. C., Burrows A., Radice D., Vartanyan D., 2019, ApJS, 241, 7

SNO + Collaboration, 2015, preprint (arXiv:1508.05759)

Sukhbold T., Ertl T., Woosley S. E., Brown J. M., Janka H. T., 2016, ApJ, 821, 38

Sukhbold T., Woosley S. E., Heger A., 2018, ApJ, 860, 93

Sumiyoshi K., Yamada S., Suzuki H., Chiba S., 2006, Phys. Rev. Lett., 97, 091101

Suwa Y., Sumiyoshi K., Nakazato K., Takahira Y., Koshio Y., Mori M., Wendell R. A., 2019, ApJ, 881, 139

Takiwaki T., Kotake K., 2018, MNRAS, 475, L91

Tamborra I., Hanke F., Müller B., Janka H.-T., Raffelt G., 2013, Phys. Rev. Lett., 111, 121104

Tamborra I., Hanke F., Janka H.-T., Müller B., Raffelt G. G., Marek A., 2014, ApJ, 792, 96

Vartanyan D., Burrows A., Radice D., Skinner M. A., Dolence J., 2018, MNRAS, 477, 3091

Vartanyan D., Burrows A., Radice D., 2019, MNRAS, 489, 2227

Walk L., Tamborra I., Janka H.-T., Summa A., 2018, Phys. Rev. D, 98, 123001

Walk L., Tamborra I., Janka H.-T., Summa A., 2019, Phys. Rev. D, 100, 063018

Walk L., Tamborra I., Janka H.-T., Summa A., 2020, Phys. Rev. D, 101, 123013

Warren M. L., Couch S. M., O'Connor E. P., Morozova V., 2019, ApJ, 898, 139

APPENDIX A: ENERGY-RESOLUTION DEPENDENCE

In this appendix, we address the energy-resolution dependence of our CCSN models by employing the 1D 19-$M_\odot$ progenitor. We ran two different simulations of 20 and 12 energy groups. This study helps us understand how the energy resolution in our 3D CCSN simulations (with 12 energy groups) affects the outcome.

In Fig. A1, we show the time evolution of neutrino luminosity and average energy. As shown in this figure, the resolution dependence is weak (a few per cent); those energy-integrated quantities are not sensitive to the energy resolution. In Fig. A2, we compare the energy flux spectra of neutrinos at the CCSN source. We find that the spectrum at peak ($\sim$10 MeV) of the 12-energy group model is slightly broader than that of the 20-energy group model and that there is a slight excess of the 12-group model at the high-energy tail in the spectrum.

Although the excess of the high-energy tail looks minor in Fig. A2, this affects the detection rate, which is shown in Fig. A3. The detection rate in the 12-energy group run is systematically higher than that of 20-energy group run. This is mainly because the cross-section of each reaction is an increasing function with energy. It should be noted, however, that the discrepancy is $\lesssim$10 per cent level, and the high-energy component in the 3D model is smaller than that of 1D (see Section 3.1 for more details), implying that the resolution dependence in 3D would be smaller than that in 1D.
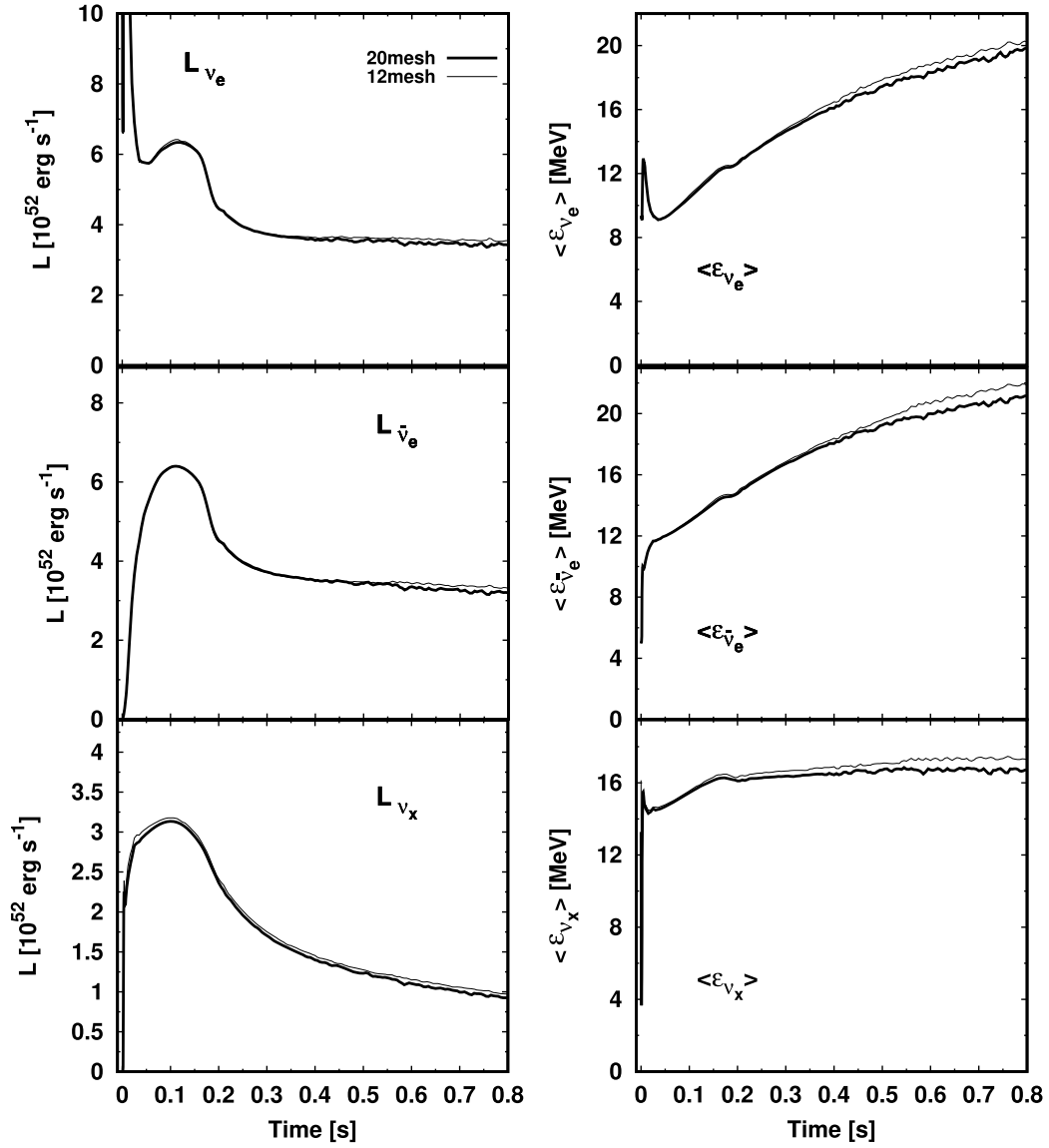
Figure A1. Same as Fig. 3 but for resolution dependence in 1D 19-$M_\odot$ models. The thick and thin lines denote the results with 20 and 12 energy groups, respectively.
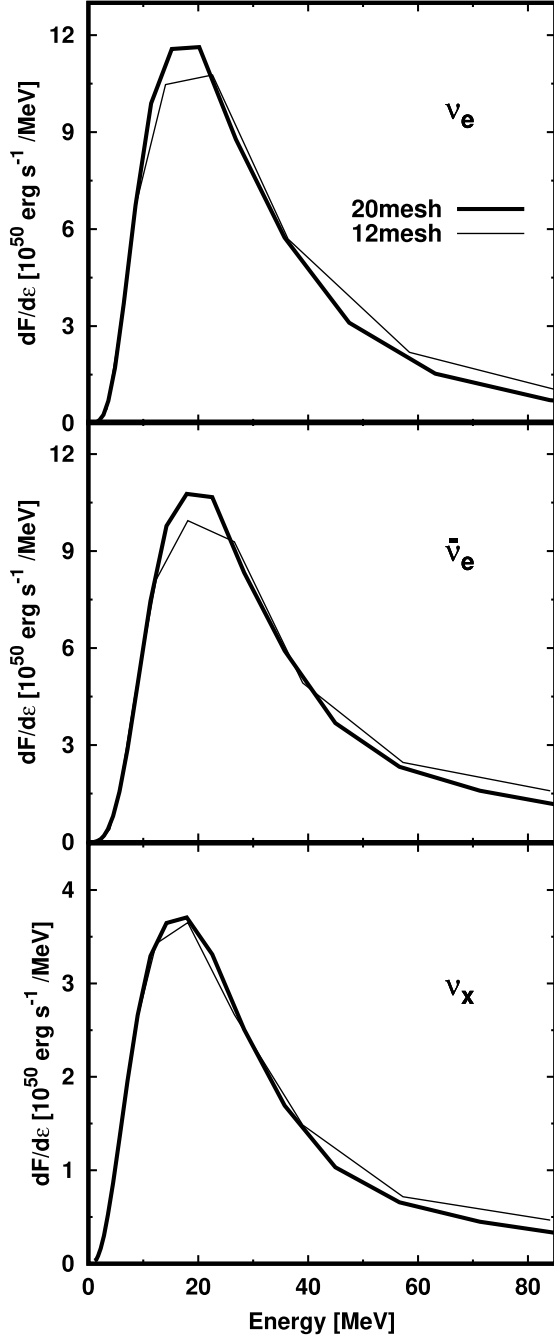
Figure A2. The energy-resolution dependence for the spectrum of neutrinos energy flux at the CCSN source for 1D 19-$M_\odot$ models. We compare the spectra at $T = 600$ ms. The thick and thin lines denote the results with 20 and 12 energy groups, respectively.
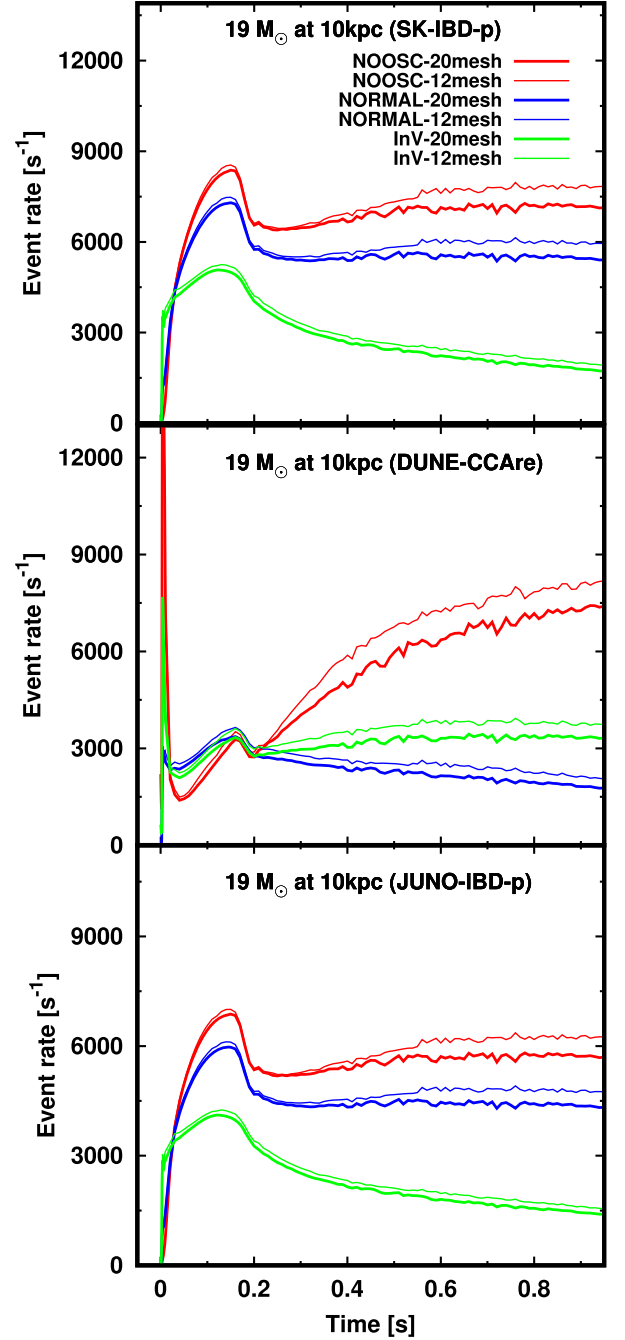
Figure A3. Same as Fig. 4 but for resolution dependence in 1D 19-$M_\odot$ model. The colour distinguishes neutrino oscillation models. The thick and thin lines denote the results with 20 and 12 energy groups, respectively.

This paper has been typeset from a T$_{E}$X/L^{A}T$_{E}$X file prepared by the author.